Computer Methods in Applied Mechanics and Engineering 450 (2026) 118602

Contents lists available at ScienceDirect

Comput. Methods Appl. Mech. Engrg.

journal homepage: www.elsevier.com/locate/cma

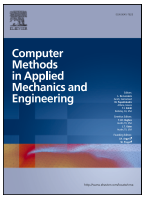

A physically consistent and quantitative phase-field model for anisotropic fracture in brittle multiphase solids

Nishant Prajapati [a,*], Lukas Schöller [b], Martin Reder [b],
Daniel Schneider [a,b,c], Britta Nestler [a,b,c]

[a] Institute of Nanotechnology - Microstructure Simulation (INT-MSS), Karlsruhe Institute of Technology, Hermann-von-Helmholtz-Platz 1, Eggenstein-Leopoldshafen, 76344, Baden-Württemberg, Germany
[b] Institute of Digital Materials Science (IDM), Karlsruhe University of Applied Sciences, Moltkestraße 30, Karlsruhe, 76133, Baden-Württemberg, Germany
[c] Institute for Applied Materials - Microstructure Modelling and Simulation (IAM-MMS), Karlsruhe Institute of Technology, Straße am Forum 7, Karlsruhe, 76131, Baden-Württemberg, Germany

ARTICLE INFO

Keywords:
Phase-field model
Brittle fracture
Anisotropic crack resistance
Orientation-invariant regularization

ABSTRACT

This work presents a physically consistent phase-field model for simulating fracture in anisotropic brittle solids, with a focus on preserving a uniform crack interface width across different phases in multiphase materials. This is achieved by incorporating anisotropy coherently into both the gradient and potential terms of the regularized crack surface energy. Theoretical relations between anisotropy parameters and critical fracture properties are systematically derived using an Iterative Graphical Method based on the Generalized Maximum Energy Release Rate criterion. Benchmark simulations confirm quantitative agreement with theory across a wide anisotropy parameter space. Compared to existing anisotropic fracture phase-field models, the present formulation shows improved predictive capabilities, quantitatively capturing both crack deflection behavior and critical energy release rates. This work serves as the first comprehensive analysis of a consistent approach to incorporating anisotropic crack resistance into phase-field fracture models, significantly enhancing their fidelity and applicability to complex multiphase materials.

1. Introduction

Understanding, predicting, and ultimately controlling crack propagation in brittle multiphase materials, comprising of several orientation-dependent solid phases, remains a central challenge in solid mechanics and materials science. Phase-field fracture models have emerged as a powerful and widely adopted numerical approach, reformulating the classical Griffith's energetic criterion [1] into a thermodynamically consistent regularized form. The foundation for phase-field modeling of brittle fracture was laid by the variational formulation of Francfort and Marigo [2] and its regularized implementation by Bourdin et al. [3]. Kuhn and Müller [4] later reinterpreted the phase-field order parameter through a Ginzburg-Landau-type evolution equation, echoing earlier formulations [5,6]. The ability of phase-field method to naturally capture crack nucleation, growth, branching, and interaction in heterogeneous media, without explicit tracking of discontinuities, has led to its widespread use in modeling fracture growth phenomena. This versatility has enabled successful extensions of the method to account for multi-field couplings, dynamic and ductile failure, hybrid (energy density degradation) formulations, mixed-mode fracture, and fatigue phenomena [7–12].

---

[*] Corresponding author.
E-mail address: nishant.prajapati@kit.edu (N. Prajapati).

https://doi.org/10.1016/j.cma.2025.118602
Received 6 August 2025; Received in revised form 10 October 2025; Accepted 21 November 2025

Available online 3 December 2025
0045-7825/© 2025 The Author(s). Published by Elsevier B.V. This is an open access article under the CC BY license (http://creativecommons.org/licenses/by/4.0/).

While classical phase-field formulations assumed isotropic fracture resistance for the sake of simplicity, many crystalline, composite and engineered materials display strong directionality in both elastic response and fracture toughness. Early efforts, to incorporate anisotropy in fracture toughness, introduced direction-dependency only in the gradient term of the surface energy density, following the strategy first used for dendritic growth by Kobayashi [13]. In line with this idea, Clayton and Knap [14,15,16] introduced a second-order structural tensor to incorporate anisotropy associated with preferred cleavage planes. This concept was further generalized by Li et al. [17], who formulated a higher order anisotropic phase-field fracture model based on a tensorial Taylor expansion to represent strongly anisotropic cubic anisotropy. Building on this approach, Teichtmeister et al. [18] employed a fourth-order structural tensor combined with Laplacian regularization to model the same symmetry class. The use of such higher-order regularization has since been explored in combination with various modeling extensions, including mesh adaptivity [19], stochastic modeling [20], FFT-based solvers [21], and orthogonal strain energy decomposition [22], enabling the simulation of experimentally observed zigzag or sawtooth crack paths, accounting for the so-called “forbidden” crack directions reported by Takei et al. [23].

Despite their conceptual simplicity, they result in orientation- and phase-dependent regularization lengths, which manifest as artificial variations in the crack interface-thickness [18,24]. Teichtmeister et al. [18] interpreted this modeling artifact as an orientation-dependent length scale, while Noii et al. [24] referred to it as an anisotropic regularization of the crack discontinuity. This modeling artifact has been reported in multiphase crack simulations of diverse polycrystalline materials [25], ranging from silicon [26] to geological media such as granite [27].

In phase-field models applied to materials science, several authors [28–32] have formulated surface energy anisotropy in a physically consistent manner to resolve the limitations of the earlier gradient-only models. These formulations incorporated anisotropy consistently in both the gradient and potential terms of the crack surface energy, thereby ensuring a uniform diffuse interface thickness and avoiding nonphysical artifacts related to orientation-dependent regularization. Tschukin et al. [33] highlighted the fundamental difference between physically consistent formulations, termed “natural", and the “classical" gradient-only approaches, and elucidated the conceptual framework for modeling surface energy anisotropy in phase-field models.

In spite of these significant advancements, this conceptual understanding has not yet been fully adopted in the fracture mechanics community. A substantial body of recent literature continues to adopt gradient-only formulations for anisotropic phase-field fracture [34–47], highlighting a persistent knowledge gap. Some prior works, including our own contributions [48–50] and a few others [51], have adopted a fully consistent treatment of anisotropy in fracture phase-field modeling. However, these studies have used different forms of the crack surface energy anisotropy function, and the broader significance and quantitative predictive capabilities of such consistent formulations remain underexplored. In particular, their applicability to multiphase systems, where phase-specific anisotropy and material properties must be incorporated alongside a common regularization length, has not yet been systematically assessed in the literature.

The present work addresses this gap by developing a physically consistent and quantitatively calibrated phase-field framework for anisotropic brittle fracture in multiphase solids. We recast a commonly used anisotropy formulation for fracture resistance, hereafter referred to as *classical* anisotropy formulation following the terminology used by Tschukin et al. [33], within the multiphase-field context and formulate the corresponding anisotropy consistently. The proposed model is systematically validated against fundamental principles of anisotropic fracture mechanics. Finally, the predictive performance of the consistent formulation is compared against the classical formulation through representative numerical examples in both single- and multiphase materials.

This article is organized as follows: Section 2 introduces the model equations, describes the procedure of derivation of theoretical relations for the proposed fracture resistance anisotropy formulation, and outlines the methodology for extracting critical fracture parameters from simulation data. Section 3 presents a detailed analysis of the theoretical relations in conjunction with the simulation results. Finally, Section 4 summarizes the key findings, offering perspectives for future research.

2. Methods

Section 2.1 outlines the phase-field model for crack growth in brittle, anisotropic multiphase solids, along with the proposed anisotropic crack resistance formulation detailed in Section 2.1.1. Section 2.2 discusses the energetic formulation for anisotropic fracture and presents the analytical expressions for the energy release rate and crack resistance anisotropy function utilized in this work. Section 2.3 describes the graphical and simulation-based approaches employed to determine the critical crack parameters.

2.0.0.1. Notation. Direct tensor notation is used throughout this work. Scalars are represented by d, D, or $\mathcal{D}$, while vectors, second-order tensors, and fourth-order tensors are denoted as $\boldsymbol{d}$, $\boldsymbol{\mathcal{D}}$, and $\mathbb{D}$, respectively. Solid phase-dependent quantities are labeled as $(*)^{\alpha}$ or $(*)_{\alpha}$ for phase-α, and crack-related quantities as $(*)_c$. The outer (dyadic) product between two vectors $\boldsymbol{c}$ and $\boldsymbol{d}$ is written as $\boldsymbol{c} \otimes \boldsymbol{d}$. The product of two second-order tensors $\boldsymbol{C}$ and $\boldsymbol{D}$ is $\boldsymbol{CD}$. The scalar (double contracted) product is $\boldsymbol{C} : \boldsymbol{D}$. A double contraction between a fourth-order tensor and a second-order tensor, yielding a second-order tensor, is written as $\mathbb{C} : \boldsymbol{C}$. In Sections 2.2, 2.3 and 3, when considering a homogeneous material, solid phase-dependent physical quantities are denoted without the phase index $(*)^{\alpha}$ for simplicity.

2.1. Multiphase-field crack model

We consider a multiphase material in a domain $\Omega \subset \mathbb{R}^d$, where $d \in \{1, 2, 3\}$, with N solid phases and a crack phase c, described by phase-fields $\varphi_{\alpha}(\mathbf{x}, t) \in [0, 1]$ for $\alpha \in \{1, \dots, N\}$ and the crack phase-field $\varphi_c(\mathbf{x}, t) \in [0, 1]$, at position $\mathbf{x}$ and time t. The solid phase-fields $\boldsymbol{\varphi}(\mathbf{x}, t) = \left\{\varphi_1(\mathbf{x}, t), \dots, \varphi_N(\mathbf{x}, t)\right\}$ satisfy the constraint $\sum_{\alpha=1}^{N} \varphi_{\alpha} = 1$. The interfaces are modeled as diffuse regions of finite width, with binary interfaces $\mathcal{I}_{\alpha\beta}$ defined by the set $\{\mathbf{x} \mid \varphi_\alpha(\mathbf{x},t) + \varphi_\beta(\mathbf{x},t) = 1, 0 < \varphi_\alpha(\mathbf{x},t) < 1\}$, and the corresponding surface is located at $\varphi_\alpha = \varphi_\beta = 0.5$. A crack phase-field of $\varphi_c = 0$ denotes completely intact material and $\varphi_c = 1$ a fully broken state. Under infinitesimal strain theory, the strain tensor reads $\boldsymbol{\varepsilon}(\mathbf{x},t) = \frac{1}{2}\left(\nabla\mathbf{u} + (\nabla\mathbf{u})^T\right)$, $\mathbf{u}(\mathbf{x},t)$ being the displacement field. The total free energy $\mathcal{F}$ of the system is expressed as

$$\mathcal{F}(\boldsymbol{\varphi},\varphi_c,\boldsymbol{\nabla}\varphi_c,\boldsymbol{\varepsilon}) = \int_\Omega f(\boldsymbol{\varphi},\varphi_c,\boldsymbol{\nabla}\varphi_c,\boldsymbol{\varepsilon})\,d\Omega = \int_\Omega \left\{f_{\mathrm{el}}(\boldsymbol{\varphi},\varphi_c,\ \boldsymbol{\varepsilon}) + f_c(\boldsymbol{\varphi},\varphi_c,\boldsymbol{\nabla}\varphi_c)\right\}d\Omega, \tag{1}$$

where the total free energy density f is the sum of the effective elastic strain energy density f_{el} and the regularized crack surface energy density f_c which is given by

$$f_c(\boldsymbol{\varphi},\varphi_c,\boldsymbol{\nabla}\varphi_c) = \frac{1}{2}\mathcal{G}_c(\boldsymbol{\varphi},\varphi_c,\boldsymbol{\nabla}\varphi_c)\Big(\frac{1}{\epsilon}w(\varphi_c) + \epsilon|\boldsymbol{\nabla}\varphi_c|^2\Big), \tag{2}$$

in terms of the effective crack resistance $\mathcal{G}_c$, regularized by the sum of a potential term $w(\varphi_c)/\epsilon$ and a gradient term $\epsilon|\boldsymbol{\nabla}\varphi_c|^2$, according to Ambrosio and Tortorelli [52], where ϵ is the regularization length scale. In this work, we employ a single-obstacle potential $w(\varphi_c) = k_w\varphi_c$, with $k_w = 9/16$ which accurately recovers the sharp crack surface energy. The effective elastic energy density and the effective crack resistance are given by:

$$f_{\mathrm{el}}(\boldsymbol{\varphi},\varphi_c,\boldsymbol{\varepsilon}) = \sum_{\alpha=1}^{N}\varphi_\alpha f_{\mathrm{el}}^\alpha(\varphi_c,\boldsymbol{\varepsilon}^\alpha), \quad \mathcal{G}_c(\boldsymbol{\varphi},\varphi_c,\boldsymbol{\nabla}\varphi_c) = \sum_{\alpha=1}^{N}\varphi_\alpha\mathcal{G}_c^\alpha(\boldsymbol{\nabla}\varphi_c) \tag{3}$$

as volumetric interpolation of the phase-dependent quantities f_{el}^α and $\mathcal{G}_c^\alpha$ using the order parameter φ_α. Following Miehe et al. [7], the phase-dependent elastic strain energy density is decomposed as follows

$$f_{\mathrm{el}}^\alpha(\varphi_c,\boldsymbol{\varepsilon}^\alpha) = (1-\varphi_c)^2\Big[f_{\mathrm{el}}^\alpha(\boldsymbol{\varepsilon}^\alpha)\Big]_+ + \Big[f_{\mathrm{el}}^\alpha(\boldsymbol{\varepsilon}^\alpha)\Big]_-, \tag{4}$$

using the tension $[\cdot]_+$ and compression $[\cdot]_-$ parts given by

$$[f_{\mathrm{el}}^\alpha(\boldsymbol{\varepsilon}^\alpha)]_\pm = \frac{1}{2}\lambda^\alpha\langle\varepsilon_1^\alpha + \varepsilon_2^\alpha + \varepsilon_3^\alpha\rangle_\pm^2 + \mu^\alpha(\langle\varepsilon_1^\alpha\rangle_\pm^2 + \langle\varepsilon_2^\alpha\rangle_\pm^2 + \langle\varepsilon_3^\alpha\rangle_\pm^2) \tag{5}$$

which represents the tension-compression split for isotropic elastic stiffness. Here, λ^α and μ^α are the phase-specific Lamé coefficients, and $\varepsilon_i^\alpha\ \forall\ i \in \{1,2,3\}$ denote the phase-specific principle strains. The operator $\langle\rangle_\pm$ represents the Macaulay brackets defined as $\langle p\rangle_\pm = (p \pm |p|)/2$ for any scalar p. This split prevents crack propagation under compression, avoiding nonphysical crack patterns. The anisotropy formulation of phase-dependent crack resistance $\mathcal{G}_c^\alpha$ and its advantages over existing approaches are detailed in Section 2.1.1. Minimizing the free energy (Eq. (1)) with respect to displacement field yields the balance of linear momentum:

$$\boldsymbol{\nabla}\cdot\left(h(\varphi_c)\bar{\boldsymbol{\sigma}}\right) = \mathbf{0}, \tag{6}$$

where $h(\varphi_c)$ is the crack degradation function defined as

$$h(\varphi_c) = \begin{cases}(1-\varphi_c)^2, & \text{if } 1-\varphi_c > \varphi_{\mathrm{residual}}\\ \varphi_{\mathrm{residual}}^2, & \text{else.}\end{cases} \tag{7}$$

This function smoothly degrades stresses in cracked regions while maintaining residual stiffness where the solid phase-field is below a threshold $\varphi_{\mathrm{residual}}$, preventing null elastic stiffness tensor and thereby ill-posedness of the linear momentum balance Eq. (6). The effective stress $\bar{\boldsymbol{\sigma}}$ is computed as a volumetric interpolation of phase-dependent stresses $\bar{\boldsymbol{\sigma}} = \sum_{\alpha=1}^{N}\varphi_\alpha\boldsymbol{\sigma}^\alpha$, with $\boldsymbol{\sigma}^\alpha = \mathbb{C}^\alpha : \boldsymbol{\varepsilon}$, using the Voigt/Taylor homogenization scheme [53]. For a detailed discussion of the various interpolation schemes used in stress calculations across interface regions, refer to Schneider et al. [54]. Under quasi-static conditions, the crack phase-field evolution follows the Allen-Cahn equation:

$$\frac{\partial\varphi_c}{\partial t} = -\frac{\mu}{\epsilon}\frac{\delta\mathcal{F}(\boldsymbol{\varphi},\varphi_c,\boldsymbol{\nabla}\varphi_c,\boldsymbol{\varepsilon})}{\delta\varphi_c} = -\frac{\mu}{\epsilon}\left(\frac{\partial f(\boldsymbol{\varphi},\varphi_c,\boldsymbol{\nabla}\varphi_c,\boldsymbol{\varepsilon})}{\partial\varphi_c} - \boldsymbol{\nabla}\cdot\frac{\partial f(\boldsymbol{\varphi},\varphi_c,\boldsymbol{\nabla}\varphi_c,\boldsymbol{\varepsilon})}{\partial\boldsymbol{\nabla}\varphi_c}\right), \tag{8}$$

where μ is a relaxation parameter, chosen sufficiently large to ensure stable relaxation of the crack phase-field φ_c to equilibrium. Note that the transient evolution of the crack phase-field (Eq. (8)) serves only as a numerical relaxation process and does not correspond to a physical time history. It represents a viscous regularization of the rate-independent problem, required for robust numerical implementation and stabilization of the simulation [55]. To prevent flux of the crack phase-field φ_c across the external boundary $\partial\Omega$, φ_c satisfies a Neumann boundary condition $\boldsymbol{\nabla}\varphi_c\cdot\boldsymbol{n} = 0$ on $\partial\Omega$, where $\boldsymbol{n}$ is the outward unit normal. Moreover, this boundary condition implies perpendicular crack intersection at the domain boundary. Since solid-solid phase transformations are not considered, the solid phase-fields are time-independent. The diffuse nature of the solid-solid interfaces ensures a smooth transition of the anisotropic crack resistance, preventing distortions in the crack phase-field that may otherwise arise from jumps in crack resistance across sharp interfaces. Moreover, if the stiffness contrast between solid phases were several orders of magnitude (not considered in this work), sharp interfaces would also induce abrupt jumps in the crack driving forces, that may lead to numerical instabilities and distortions in the crack phase-field.

Staggered solution scheme. The governing Eqs. (6) and (8) are solved using a staggered scheme, outlined in Algorithm 1. For a multiphase domain with an initial crack and diffuse interfaces (including crack surfaces and grain boundaries), these equations are solved iteratively at each boundary increment (e.g., displacement or traction) until the crack phase-field reaches steady state. A boundary increment denotes either a displacement increment in a Dirichlet-type incremental displacement boundary condition or a traction increment in a Neumann-type incremental traction boundary condition. Steady state is defined when the domain-averaged L_2-norm of the crack phase-field φ_c change between successive time steps, t_n and t_{n+1} falls below a tolerance ϵ_{φ_c}. This is mathematically expressed as

$$\left(\frac{1}{V_\Omega}\int_\Omega (\varphi_c(\mathbf{x},t_{n+1})-\varphi_c(\mathbf{x},t_n))^2\,d\Omega\right)^{1/2} < \epsilon_{\varphi_c}, \tag{9}$$

V_Ω being the domain volume. This condition ensures that the crack evolution has effectively ceased and the crack phase has relaxed to its equilibrium state. After reaching steady state, the next load increment is applied. The simulation ends either when the material is fully cracked or after the final load increment and subsequent steady state. Crack growth is modeled as a quasi-static process, where time steps in the crack evolution equation represent relaxation steps for the crack to reach equilibrium under a given load increment, rather than physical time. The intermediate stages of crack evolution therefore represent numerical relaxation states without any physical time associated. Physical time can be associated only with time-dependent boundary conditions.

Algorithm 1: Staggered Solution Scheme.

```
Initialize $\boldsymbol{\varphi}_s, \varphi_c$;
Initialize boundary condition;
Initialize simEnded, steadyState, lastLoadIncrement, fullyCracked to False;
while not simEnded do
    Solve linear momentum balance: $\boldsymbol{u} \leftarrow \nabla \cdot \left(h(\varphi_c)\,\bar{\boldsymbol{\sigma}}(\boldsymbol{u})\right) = \mathbf{0}$;
    Solve crack evolution equation: $\varphi_c \leftarrow \varphi_c + \Delta t \cdot \dot{\varphi}_c$;
    steadyState $\leftarrow \|\dot{\varphi}_c\|_2 < \epsilon_{\varphi_c}$;
    if steadyState then
        Increment boundary load;
        lastLoadIncrement $\leftarrow$ Check for end of loading;
        fullyCracked $\leftarrow \left(f_{\mathrm{el}} < \epsilon_{\mathrm{residual}}\right)$;
        if lastLoadIncrement or fullyCracked then
            simEnded $\leftarrow$ True;
        steadyState $\leftarrow$ False;
```

Numerical discretization. The crack evolution Eq. (8) is solved using an explicit Euler method for time integration, while the stationary balance of linear momentum Eq. (6) is solved to equilibrium in each pseudo-time step. An equidistant Cartesian grid is employed for spatial discretization. Regarding the crack evolution and the corresponding fluxes, i.e. $\nabla \cdot (\partial f/\partial \nabla\varphi_c)$, a cell centered finite volume discretization with second order schemes is used. For the momentum balance Eq. (6), a rotated staggered discretization is employed where the displacements are stored at grid nodes, while stresses are evaluated at cell centers. This setup corresponds to a regular finite element mesh with uniformly sized linear elements and full integration. The resulting linear equation system is solved using the *Conjugate Gradient Method*.

Computational aspects. During each relaxation step Δt, the local condition $\dot{\varphi}_c \geq 0$ is enforced to ensure irreversibility. The latter is implemented via a Dirichlet-type constraint [56], following Schöller et al. [57]. The material is considered fully damaged ($\varphi_c = 1$), when the crack phase-field reaches the critical value $\varphi_c^{\mathrm{critical}} = 1 - \epsilon_{\mathrm{damage}}$, $\epsilon_{\mathrm{damage}}$ denoting a damage tolerance. This approach improves numerical behavior while having negligible impact on the results. Alternative strategies for enforcing irreversibility in the present model include the strain-history function [55], augmented Lagrangian method [58], primal-dual active-set approach [59], complementarity systems [60], or interior point methods [61].

The model is implemented in the PACE3D multiphysics simulation framework [62], written in C. The solver is highly parallelized using message passing interface (MPI) standard, incorporating domain decomposition and dynamic redistribution schemes, enabling large-scale simulations of multiphase composite materials containing numerous solid phases with varying material properties. Simulations in this work were performed on a high-performance work station using multiple CPUs.

2.1.1. *Anisotropic crack resistance: root-squared-orthotropic formulation*

We introduce a *Root-Squared-Orthotropic* anisotropy function for the phase-specific crack resistance:

$$\mathcal{G}_c^\alpha(\nabla\varphi_c) = \sqrt{\left(\boldsymbol{\mathcal{G}}_c^\alpha\right)^2 : (\boldsymbol{n}_c \otimes \boldsymbol{n}_c)}, \tag{10}$$

where, $\boldsymbol{n}_c = -\nabla\varphi_c/|\nabla\varphi_c|$ is the unit crack phase-field gradient vector. In the fully intact solid regions where $\varphi_c = 0$, and hence the gradient vector $\nabla\varphi_c = \mathbf{0}$, $\boldsymbol{n}_c$ is not defined. For numerical implementation, $\boldsymbol{n}_c$ is set to $\mathbf{0}$ in these regions, ensuring that the terms involving $\boldsymbol{n}_c$ in the evolution equation (Eq. (8)) vanish, preventing spurious contributions outside the crack regions and avoiding singularities that would otherwise arise from the normalization of gradient vector. The anisotropic phase-specific crack resistance tensor reads

$$\boldsymbol{\mathcal{G}}_c^{\alpha} = \boldsymbol{Q}_{\alpha}\boldsymbol{\mathcal{G}}_{c_0}^{\alpha}\boldsymbol{Q}_{\alpha}^{T}, \tag{11}$$

with $\boldsymbol{Q}_{\alpha}$ being the phase-dependent rotation tensor describing the crystallographic orientation of phase α, and

$$\boldsymbol{\mathcal{G}}_{c_0}^{\alpha} = \mathcal{G}_{c_0 i}^{\alpha}(\hat{\boldsymbol{e}}_i \otimes \hat{\boldsymbol{e}}_i) = \mathrm{diag}\left(\mathcal{G}_{c_0 1}^{\alpha}, \mathcal{G}_{c_0 2}^{\alpha}, \mathcal{G}_{c_0 3}^{\alpha}\right) \tag{12}$$

is the reference crack resistance tensor, representing the crack resistance normal to the principal directions $\hat{\boldsymbol{e}}_i$ of the crystallographic coordinate system of phase-α. This formulation captures direction-dependent crack resistance in anisotropic solids, especially where fracture properties vary along orthogonal directions. The phase-specific anisotropy strength in 2D is defined as

$$\mathcal{S}^{\alpha} = \left(\frac{\mathcal{G}_{c_0 1}^{\alpha}}{\mathcal{G}_{c_0 2}^{\alpha}}\right)^2, \tag{13}$$

reflecting the squared nature of the tensor projection. The present anisotropy formulation (Eq. (2), Eqs. (10)-(12)) offers a physically consistent alternative to a commonly used anisotropic model, which is discussed in the following.

2.1.1.1. *Comparison with a Commonly Used Anisotropic Formulation.*

A widely used anisotropic phase-field formulation [14–16] incorporates anisotropy solely through the gradient term using a second-order structural tensor:

$$\boldsymbol{\omega} = \mathbf{1} + \beta(\mathbf{1} - \boldsymbol{m} \otimes \boldsymbol{m}), \tag{14}$$

where $\mathbf{1}$ denotes the second order identity tensor, $\boldsymbol{m}$ is the cleavage plane normal vector and β is the energetic penalty factor that controls the anisotropy strength. This modifies the gradient contribution as:

$$|\nabla\varphi_c|^2 \rightarrow \boldsymbol{\omega} : (\nabla\varphi_c \otimes \nabla\varphi_c). \tag{15}$$

Increasing the value of β increasingly penalize propagation directions that are not orthogonal to $\boldsymbol{m}$. Despite its computational simplicity, this gradient-only approach, here referred as *classical formulation*, introduces two major artifacts:

1. Physically inconsistent alteration of crack surface energy.
2. Orientation- and phase-dependent variation in crack interface width, especially problematic in multiphase systems.

These issues have been observed but largely unaddressed in the literature [18,24,63]. While some authors interpret the interface width variation as an effective orientation-dependent length scale or anisotropic regularization, it remains a modeling artifact. To enable a direct comparison, we recast the *classical formulation* in the present multiphase-field framework. The corresponding crack surface energy density reads:

$$\tilde{f}_c(\boldsymbol{\varphi}, \varphi_c, \nabla\varphi_c) = \underbrace{\frac{1}{2\epsilon}\tilde{\mathcal{G}}_c^0(\boldsymbol{\varphi})w(\varphi_c)}_{\text{isotropic}} + \underbrace{\frac{\epsilon}{2}\tilde{\mathcal{G}}_c(\boldsymbol{\varphi}, \nabla\varphi_c)|\nabla\varphi_c|^2}_{\text{anisotropic}}, \tag{16}$$

with volumetric interpolation:

$$\tilde{\mathcal{G}}_c^0(\boldsymbol{\varphi}) = \sum_{\alpha=1}^{N} \varphi_\alpha \tilde{\mathcal{G}}_c^{\alpha,0}, \quad \tilde{\mathcal{G}}_c(\boldsymbol{\varphi}, \nabla\varphi_c) = \sum_{\alpha=1}^{N} \varphi_\alpha \tilde{\mathcal{G}}_c^{\alpha}(\nabla\varphi_c), \tag{17}$$

where $\tilde{\mathcal{G}}_c^{\alpha,0}$ denotes the isotropic part of the crack resistance for phase α, while $\tilde{\mathcal{G}}_c^{\alpha}(\nabla\varphi_c)$ represents the anisotropic contribution given by:

$$\tilde{\mathcal{G}}_c^{\alpha}(\nabla\varphi_c) = \boldsymbol{\mathcal{G}}_c^{\alpha} : (\boldsymbol{n}_c \otimes \boldsymbol{n}_c), \quad \boldsymbol{n}_c = -\frac{\nabla\varphi_c}{|\nabla\varphi_c|}. \tag{18}$$

This structure is analogous to the earlier tensor-based formulation (Eq. (14)) and is equivalent to that used by Li and Maurini [63] for single-phase materials. The tensor $\boldsymbol{\mathcal{G}}_c^{\alpha}$ here is analogous to (phase-specific) projection tensor $\boldsymbol{\omega}^{\alpha}$ in the classical formulation, and their $\boldsymbol{m}^{\alpha}$ is related to our phase-specific rotation tensor $\boldsymbol{Q}^{\alpha}$. In two dimensions, the anisotropy strength $\mathcal{S}^{\alpha}$ is also equivalent to (phase-specific) β^{α} in $\boldsymbol{\omega}^{\alpha}$. While the classical formulation yields an orthotropic anisotropy, the consistent formulation introduced in this work adopts a *Root-Squared Orthotropic* form. The consistent formulation avoids artificial direction-dependent effects at the crack interface and allows for a direct comparison between the two classes of anisotropy models, similar to the “classical” versus “natural” modeling approaches discussed by Tschukin et al. [33] for interfacial anisotropy. Fig. 1 compares the crack interface profiles obtained from both formulations for different anisotropy strengths $\mathcal{S} \in \{1, 10\}$ and crystal orientations $\tilde{\theta} \in \{0°, 45°, 90°\}$. Since a single-phase solid is considered, phase-specific $(*)^{\alpha}$ notation is omitted. Notably, the crack phase-field φ_c near the crack tip adapts to the local crystal orientation in both formulations. However, the classical formulation shows varying interface widths depending on $\mathcal{S}$ and $\tilde{\theta}$, narrowing for $\mathcal{S} = 0.1$ and widening for $\mathcal{S} = 10$ as $\tilde{\theta}$ increases. The consistent formulation, on the other hand, maintains a uniform interface width, eliminating artificial direction-dependent effects. This uniformity is essential for accurately capturing the crack energetics, especially in multiphase systems with strong directional behavior.

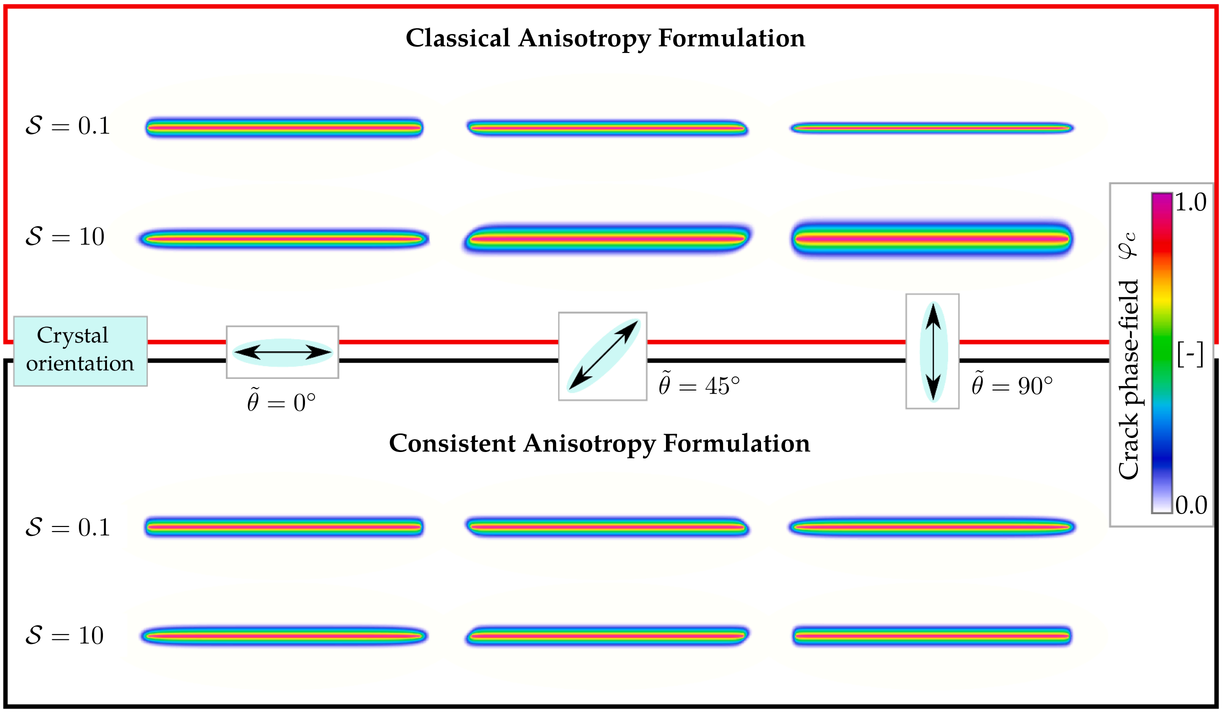

Fig. 1. Comparison of crack interface profiles represented by the crack phase-field φ_c computed using the classical anisotropy formulation and the consistent formulation of this work. Results are shown for anisotropy strengths $\mathcal{S} = 0.1$ and 10, and crystal orientations $\tilde{\theta} \in \{0°, 45°, 90°\}$ (indicated by arrows). The classical formulation exhibits a strong dependence of the crack interface width on both $\mathcal{S}$ and $\tilde{\theta}$, while the consistent formulation maintains a uniform interface width across all orientations and anisotropy strengths.

2.2. *Energetics and analytical expressions for anisotropic fracture*

2.2.1. *Energetics*

In this section, we consider the energetics of anisotropic fracture in homogeneous solids, omitting phase-specific $(*)^\alpha$ notation for clarity. Fracture growth follows Griffith's criterion [1], where a crack advances when the energy release rate $\mathcal{G}(\theta)$ reaches the critical value $\mathcal{G}_c(\theta;\tilde{\theta})$, i.e. $\mathcal{G}(\theta) = \mathcal{G}_c(\theta;\tilde{\theta})$. Under this condition, and assuming quasi-static loading, the crack path is governed by the Generalized Maximum Energy Release Rate (GMERR) criterion:

$$\theta^* = \underset{\theta\in[0,2\pi)}{\arg\max} \frac{\mathcal{G}(\theta)}{\mathcal{G}_c(\theta;\tilde{\theta})}, \tag{19}$$

where θ is the polar angle defining the crack direction, $\tilde{\theta}$ denotes the crystal orientation, and the solution θ^* corresponds to the kink angle. This maximization problem leads to the first-order optimality condition: $\dfrac{d\mathcal{G}(\theta)}{d\theta} = \dfrac{\partial \mathcal{G}_c(\theta;\tilde{\theta})}{\partial\theta}$, which physically represents the balance of configurational torque at the crack tip [64]. Well-posedness of the governing (Allen-Cahn-type) phase-field evolution equation (Eq. (8)) resulting from the variational formulation requires angle-convexity of the Frank-plot (i.e. polar plot of the reciprocal function) of crack resistance (see Taylor and Cahn [65]), which is ensured by the second-order condition:

$$\frac{\partial^2 \mathcal{G}_c(\theta;\tilde{\theta})}{\partial\theta^2} + \mathcal{G}_c(\theta;\tilde{\theta}) \geq 0. \tag{20}$$

Materials satisfying this condition are referred to as weakly anisotropic, while those that do not are termed strongly anisotropic [17,18]. For the latter class, Li et al. [17] demonstrated that introducing higher-order Laplacian term in the surface energy regularization restores well-posedness of the governing equations, and allows modeling of forbidden crack directions [23], leading to saw-tooth crack patterns, as also confirmed by later works [18,63]. Graphical construction by Gurtin and Podio-Guidugli [66] provides a convenient methodology for predicting crack direction, for both weakly and strongly anisotropic materials, by superimposing the Frank plots of $\mathcal{G}_c(\theta;\tilde{\theta})$ and $\mathcal{G}(\theta)$. For a given mode-mixity, the minimum mode I stress intensity factor K_I satisfying the tangency condition between the two plots determines both the critical energy release rate $\mathcal{G}_c^*$ and the kink angle θ^*. As loading increases, the plot of $1/\mathcal{G}(\theta)$ moves toward the origin until it becomes tangent to the fixed $1/\mathcal{G}_c(\theta;\tilde{\theta})$ plot. This procedure is illustrated in Fig. 2a,b.

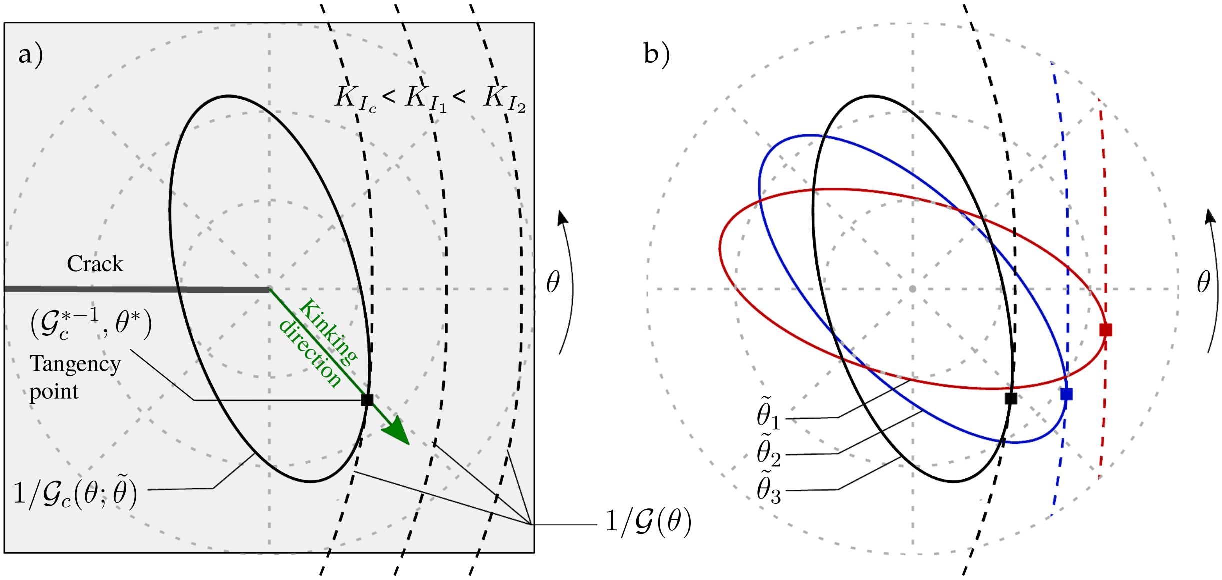

Fig. 2. a) Schematics illustrating the determination of critical crack parameters, i.e. critical energy release rate $\mathcal{G}_c^*$ and crack kink angle θ^*, based on the point of tangency between the polar plots of the reciprocal crack resistance $1/\mathcal{G}_c$ and the energy release rate $1/\mathcal{G}$. The lowest mode I stress intensity factor K_I at which the two curves become tangent determines the critical crack parameters $(\mathcal{G}_c^*, \theta^*)$ and the mode-I critical stress intensity factor K_{I_c}. b) Schematic illustrating the determination of critical crack parameters for different crystal orientations $\tilde{\theta}_i$ using the graphical method.

2.2.2. *Analytical expressions*

2.2.2.1. Anisotropic Crack Resistance. For a homogeneous solid in two dimensions, the *Root-Squared-Orthotropic* anisotropy function for crack resistance (Eq. (10)), omitting phase-specific notation $(*)^\alpha$ for clarity, is given by:

$$\mathcal{G}_c(\theta; \tilde{\theta}) = \sqrt{\mathcal{G}_{c_01}^2 \sin^2\left(\theta - \tilde{\theta}\right) + \mathcal{G}_{c_02}^2 \cos^2\left(\theta - \tilde{\theta}\right)}. \tag{21}$$

Here, θ is the crack orientation, defined as the angle between the crack tangent and the global x-axis, while $\tilde{\theta}$ denotes the crystal orientation of the material relative to the global frame. The reference crack resistances $\mathcal{G}_{c_{01}}$ and $\mathcal{G}_{c_{02}}$ correspond to the values normal to the local crystallographic x- and y-directions, respectively. The anisotropy strength is defined as $\mathcal{S} := \mathcal{G}_{c_{01}}^2/\mathcal{G}_{c_{02}}^2$, with $\mathcal{S} \in (0, \infty)$ to satisfy the convexity condition (Eq. (20)). A detailed derivation of Eq. (21) is provided in A.

Figs. 3a,b depict the polar plots of the normalized crack resistance $\mathcal{G}_c(\theta; \tilde{\theta})/\mathcal{G}_0$ (with $\mathcal{G}_{c_02} = \mathcal{G}_0$) and its reciprocal, the Frank plot, for various values of anisotropy strength $\mathcal{S}$ and crystal orientation $\tilde{\theta}$. It should be noted that while the polar plots of normalized crack resistance can be non-convex depending on $\mathcal{S}$, but the Frank plots remain convex for all $\mathcal{S} \in (0, \infty)$. At $\mathcal{S} = 1$, both plots reduce to unit circles (black curves), indicating isotropic crack resistance. For $\mathcal{S} > 1$, crack resistance increases away from the crystal direction, peaking orthogonally, see blue-shaded curves in Fig. 3a, thereby penalizing crack growth in directions other than the crystal orientation. Conversely, for $\mathcal{S} < 1$, resistance decreases in those directions, favoring orthogonal crack growth (red-shaded curves). The Frank plots in Fig. 3b exhibit the inverse trends, as expected, and serve as a useful tool for determining the critical energy release rate $\mathcal{G}_c^*$ and kink angle θ^*, discussed in Section 2.2.1.

2.2.2.2. Energy release rate. Amestoy and Leblond [67] derived a closed-form expression for the energy release rate, $\mathcal{G}(\theta)$, of a crack kinking at an angle θ with vanishing extension length:

$$\mathcal{G}(\theta) = \frac{\tilde{K}_I^2(\theta) + \tilde{K}_{II}^2(\theta)}{E'}, \tag{22}$$

where E' is the effective Young's modulus, and $\tilde{K}_I$, $\tilde{K}_{II}$ are the effective stress intensity factors for modes I and II. For completeness, detailed expressions are provided in B.

2.3. *Determination of critical crack parameters*

The phase-specific notation $(*)^\alpha$ is omitted in this section for clarity, as the discussion is restricted to a homogeneous solid.

2.3.1. *Analytical determination via an iterative graphical method*

To determine the critical energy release rate $\mathcal{G}_c^*$ and the crack kink angle θ^* for anisotropic crack resistance, we employed what we refer to as the *Iterative Graphical Method*, based on the graphical approach of Gurtin and Podio-Guidugli [66]. Using the analytical

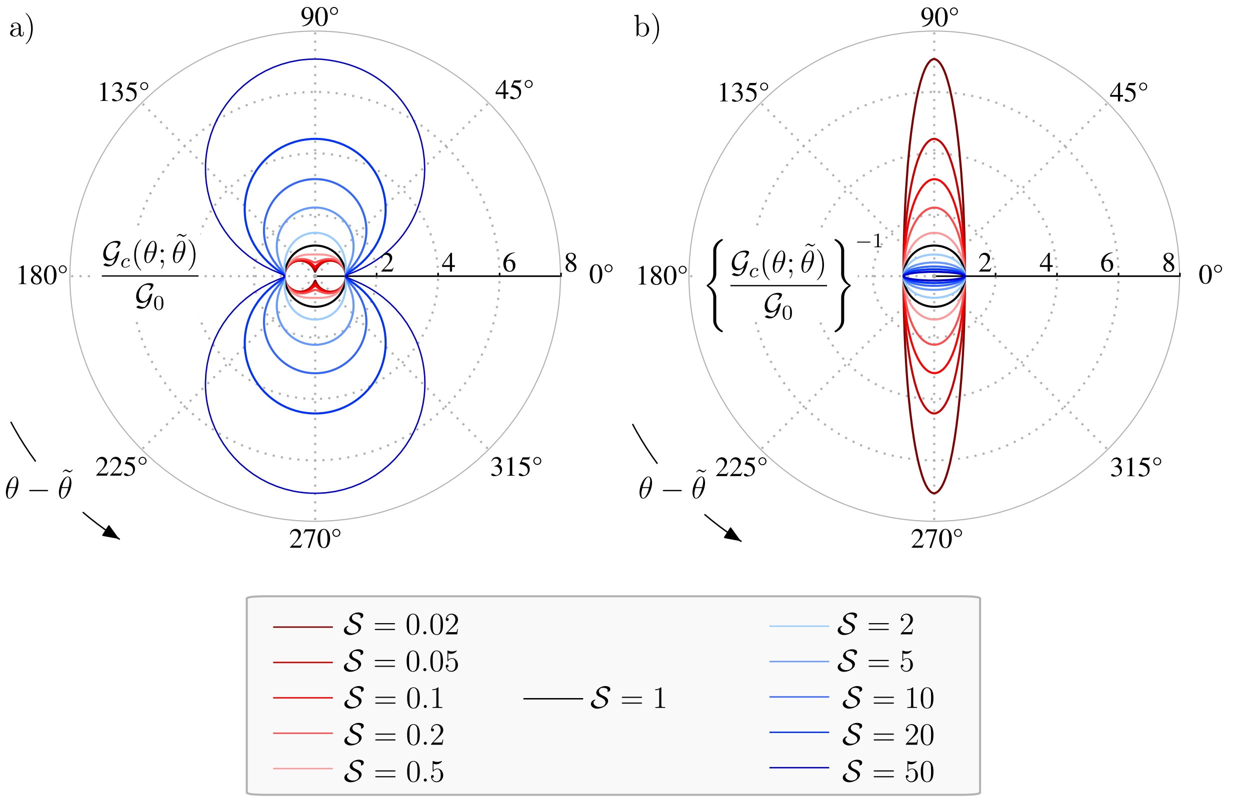

Fig. 3. Polar plots showing the angular variation of the normalized crack resistance $\mathcal{G}_c(\theta;\tilde{\theta})/\mathcal{G}_0$, with respect to the crystal orientation $\tilde{\theta}$, along with its reciprocal, $\{\mathcal{G}_c(\theta;\tilde{\theta})/\mathcal{G}_0\}^{-1}$, for different values of anisotropy strength $\mathcal{S}$. The reciprocal function is also referred to as the Frank plot of the normalized crack resistance.

expressions (Eqs. (21) and (22)) from previous sections, we construct polar plots of $1/\mathcal{G}(\theta)$ and $1/\mathcal{G}_c(\theta;\tilde{\theta})$. Starting with a sufficiently large mode-I stress intensity factor K_I, such that the plot of $1/\mathcal{G}(\theta)$ lies entirely outside the $1/\mathcal{G}_c(\theta;\tilde{\theta})$-plot, K_I is iteratively reduced until the curves become tangent. This tangency yields both $\mathcal{G}_c^*$ and θ^*, as illustrated in Fig. 2a. The resulting relations connect anisotropy strength $\mathcal{S}$, crystal orientation $\tilde{\theta}$, and critical crack parameters $\mathcal{G}_c^*$ and θ^*, across different anisotropy formulations and crystal orientations, schematically illustrated in Fig. 2b.

2.3.2. Numerical estimation from simulations

2.3.2.1. Kink Angle. The kink angle is estimated from a grayscale snapshot of the phase-field at the critical load step, where $\varphi_c = 1.0$ (white) denotes fully broken regions and $\varphi_c = 0.0$ (black) indicates intact material, see Fig. 4a. The image is lightly smoothed using a Gaussian filter to reduce mesh-induced pixelation while preserving crack features. The initial crack tip is identified as the rightmost pixel with $\varphi_c \geq 0.95$ in the pre-kink image (blue dot in Fig. 4a). Using this as a reference, a small window around the kinked region is extracted, and the brightest pixels within are used to fit a straight line. The orientation of this line determines the kink angle.

2.3.2.2. Critical Energy Release Rate. To estimate the critical mode I stress intensity factor K_{I_c}, and the corresponding critical energy release rate $\mathcal{G}_c^*$, the *Displacement Extrapolation Method* (e.g., Zhu and Oterkus [68]) was employed. At the critical load step corresponding to simulated crack kinking, vertical displacements u_y were extracted along the upper and lower crack surfaces near the crack tip. The crack opening displacement (COD), denoted Δu_y, was computed as the difference between the displacements across these faces within a narrow region adjacent to the crack tip, as illustrated in Fig. 4b. Measurements were taken at four grid points adjacent to the tip. These COD values were then used to extrapolate K_{I_c} based on the linear elastic fracture mechanics formulation. Details of the mathematical procedure and relevant expressions for extracting K_{I_c} and computing the simulation-based critical energy release rate $\mathcal{G}_{c,\mathrm{sim}}^*$ are provided in C.

3. Results and discussion

Section 3.1 provides an in-depth analysis of the theoretical findings correlating anisotropic material properties with critical crack parameters across a broad parameter space. These relationships are validated through numerical simulations in Section 3.2. Section 3.3 offers a detailed investigation of the resulting anisotropic mechanical behavior predicted by the model. Finally, Section 3.4 presents an elaborate comparative analysis between the proposed *consistent* anisotropy formulation and the widely used *classical* approach.

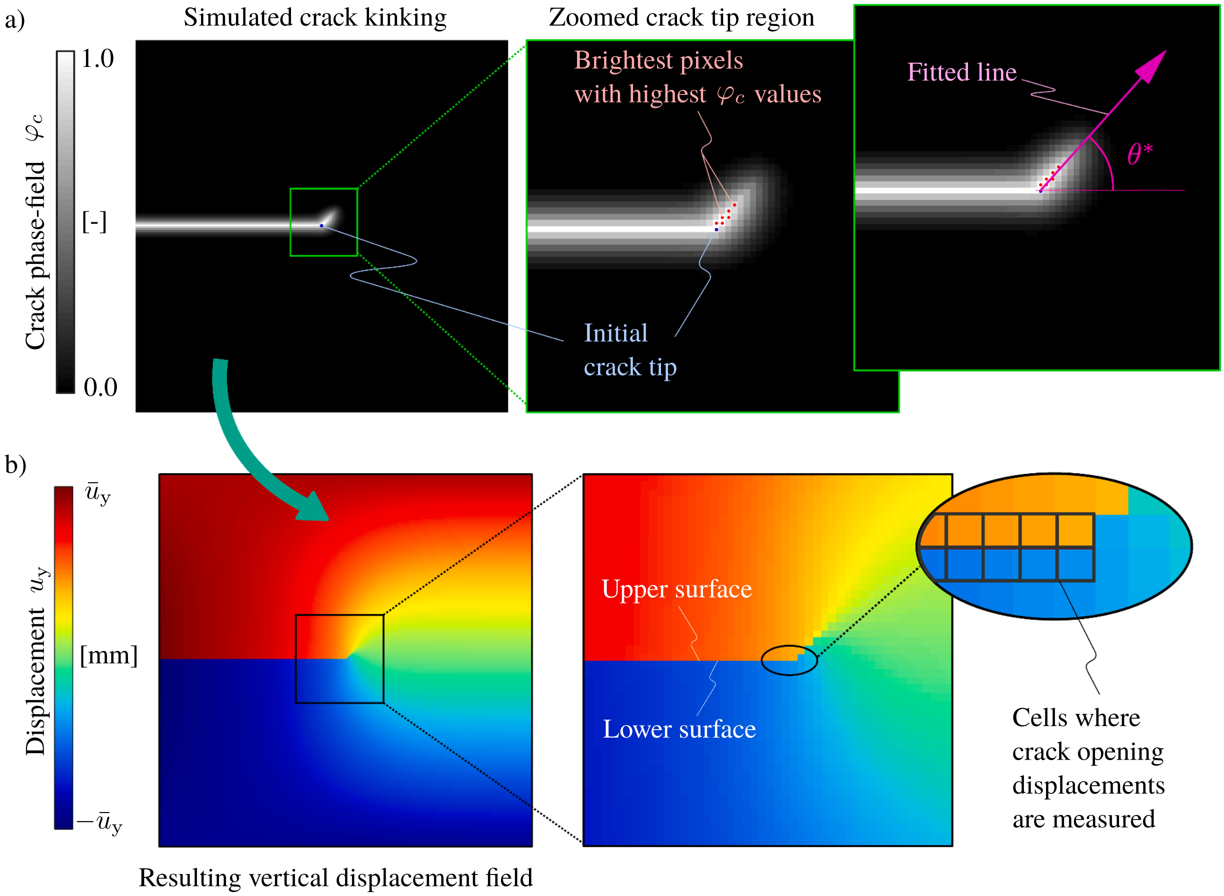

Fig. 4. (a) Schematic illustration of kink angle estimation θ^*. A small window near the initial crack tip is extracted from the grayscale image of the simulated crack phase-field at the critical load step. The brightest pixels are identified, and a straight line is fitted through these points and the initial crack tip to determine the kink angle θ^*. (b) Schematic of critical energy release rate estimation $\mathcal{G}_c^*$ from the vertical displacement field u_y, with $\pm\bar{u}_y$ indicating the boundary displacements. At the critical load step, crack opening displacements are measured at selected cells near the crack tip. Critical mode-I stress intensity factor K_{I_c} and critical energy release rate $\mathcal{G}^*_{c,\mathrm{sim}}$ are computed using the Displacement Extrapolation Method.

3.1. *Theoretical relations between anisotropy and critical crack properties*

Using the *Iterative Graphical Method* discussed in Section 2.3.1, we determine the critical crack parameters–the critical energy release rate $\mathcal{G}_c^*$ and kink angle θ^*–for varying anisotropy strength $\mathcal{S}$ and crystal orientation $\tilde{\theta}$.

3.1.1. *Critical crack parameters in a broad material anisotropy regime*

Fig. 5 depicts the loci of critical crack parameters in polar coordinates as functions of the anisotropy strength $\mathcal{S}$ for various crystal orientations $\tilde{\theta}$. The radial coordinate represents the reciprocal of the normalized critical energy release rate $\left\{\mathcal{G}_c^*/\mathcal{G}_0\right\}^{-1}$, while the angular coordinate corresponds to the kink angle θ^*. Surrounding the central plot, the polar-plots display the reciprocal normalized crack resistance $\left\{\mathcal{G}_c(\theta;\tilde{\theta})/\mathcal{G}_0\right\}^{-1}$ (solid elliptical curves) and the reciprocal energy release rate $\mathcal{G}(\theta)^{-1}$ (dotted lines). Tangency points between these curves identify the critical parameters $\left\{\mathcal{G}_c^*/\mathcal{G}_0\right\}^{-1}$ and θ^*, as determined by the *Iterative Graphical Method*, across combinations of $\tilde{\theta}$ and $\mathcal{S}$. At $\mathcal{S} = 1$, all tangency points coincide at $\theta = 0°$, indicating horizontal crack propagation independent of crystal orientation. For $\mathcal{S} < 1$, the kink angle lies in the fourth quadrant, reflecting negative crack deflections. In this regime, decreasing $\mathcal{S}$ lowers resistance in directions perpendicular to the crystallographic axis, thereby directing the crack path toward the perpendicular direction. Conversely, for $\mathcal{S} > 1$, θ^* shifts into the first quadrant for all $\tilde{\theta} \in (0°, 90°)$, as highlighted in the zoomed inset. In this regime, the critical energy release rate exhibits a non-monotonic dependence on $\mathcal{S}$, a behavior explored further in the following sections.

3.1.2. *Influence of anisotropy strength*

Fig. 6a,b depicts the variation of the normalized critical energy release rate $\mathcal{G}_c^*/\mathcal{G}_0$ and crack kink angle θ^* as functions of anisotropy strength $\mathcal{S}$ for different crystal orientations $\tilde{\theta}$. Quadratic B-spline interpolation was used to smoothen the discrete dataset and capture the continuous physical trends. The resulting plots can be classified into three regimes:

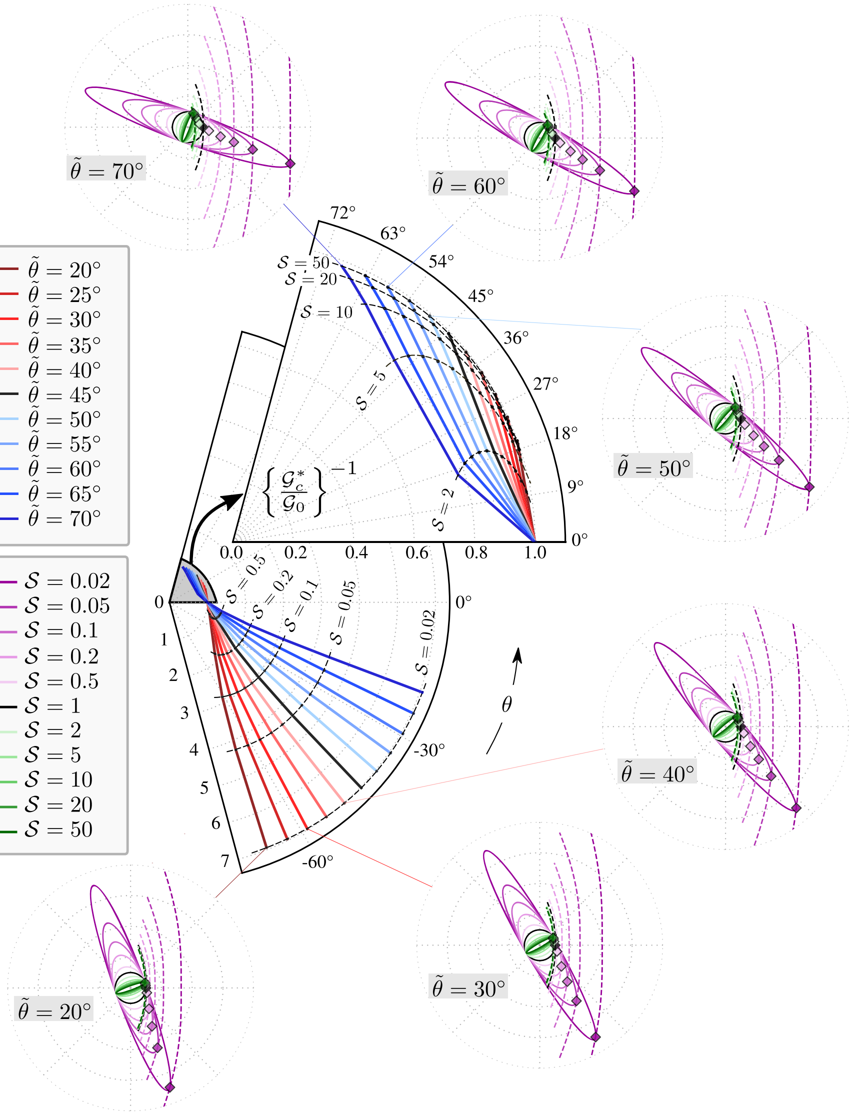

Fig. 5. Central polar plots showing the loci of tangency points that define the reciprocal normalized critical energy release rate $\{\mathcal{G}_c^*/\mathcal{G}_0\}^{-1}$, and the corresponding kink angle θ^* as functions of anisotropy strength $\mathcal{S}$ for various crystal orientations $\tilde{\theta}$. A zoomed inset highlights the plots in the first quadrant. The surrounding outer polar plots display the Frank plots of anisotropic crack resistance and energy release rate for selected values of $\mathcal{S}$ and $\tilde{\theta}$ for which the tangency condition is met, as determined using the *Iterative Graphical Method*.

- *Isotropic Case* ($\mathcal{S} = 1$):
  This case corresponds to the common intersection point of all curves in Fig. 6a,b, where $\mathcal{G}_c^*/\mathcal{G}_0 = 1$ uniformly across all crystal orientations $\tilde{\theta}$. This indicates that the critical energy release rate $\mathcal{G}_c^*$ matches the isotropic reference value $\mathcal{G}_0$, independent of $\tilde{\theta}$. Kink angles also vanish for all $\tilde{\theta}$, indicating horizontal crack propagation without deflection.
- *Lower Anisotropy Regime* ($\mathcal{S} < 1$):
  In this regime (magenta-shaded region in Fig. 6a), $\mathcal{G}_c^*/\mathcal{G}_0$ increases monotonically with $\mathcal{S}$, but decreases with increasing $\tilde{\theta}$. At very low $\mathcal{S}$, θ^* approaches directions orthogonal to the crystal orientation, see zoomed insets in Fig. 6b. In the approximate range $\mathcal{S} \lesssim 0.28$ (white region, right-bounded by the red dashed line), θ^* increases with orientation. This trend reverses in the intermediate range $0.28 \lesssim \mathcal{S} < 1$ for $\tilde{\theta} < 45°$, where higher $\tilde{\theta}$ leads to smaller θ^*, see yellow-shaded region in the smaller inset of Fig. 6b.
- *Upper Anisotropy Regime* ($\mathcal{S} > 1$):
  Here, $\mathcal{G}_c^*/\mathcal{G}_0$ increases with $\mathcal{S}$, peaking within $\mathcal{S} \in (2, 5)$ as shown in gray-shaded region in Fig. 6a, then gradually decreases, asymptotically approaching unity for all crystal orientations $\tilde{\theta}$. The peaks indicate optimal values of anisotropy strength, $\mathcal{S}_{\text{Peak}}$, where the crack resistance is maximum. For $\mathcal{S} \gtrsim 3.7$ (region to the right of blue-dashed line in larger inset of Fig. 6b), θ^* increases

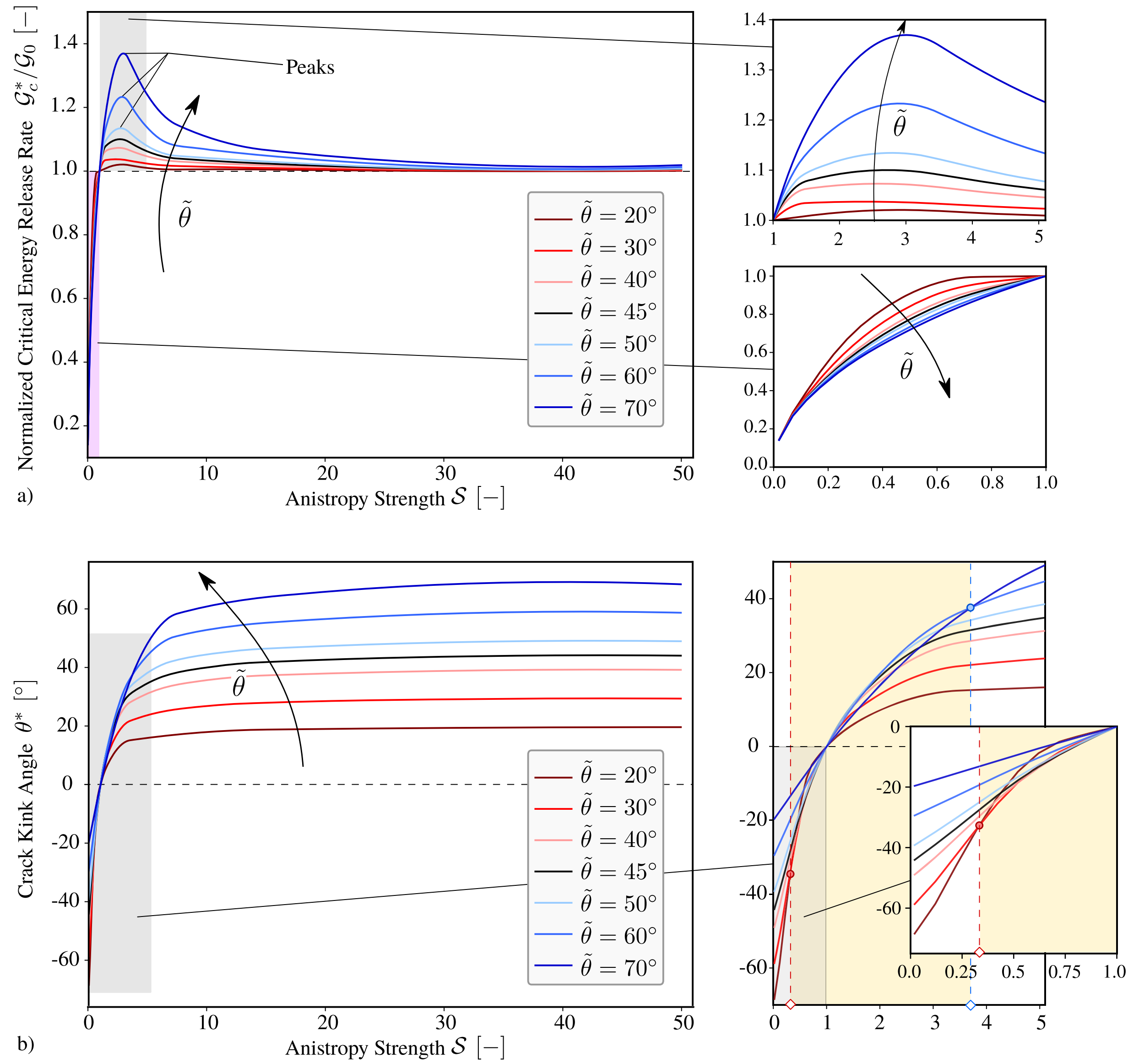

Fig. 6. Plots of a) normalized critical energy release rate $\mathcal{G}^*/\mathcal{G}_0$, and b) crack kink angle θ^* as a function of anisotropy strength $\mathcal{S}$, for different values of the orientation $\tilde{\theta}$. The inset plots illustrates the zoomed plots in different ranges of $\mathcal{S}$.

with $\tilde{\theta}$ and approaches it asymptotically for larger values of $\mathcal{S}$, yielding nearly horizontal curves. In the intermediate regime $1 < \mathcal{S} \lesssim 3.7$ and for $\tilde{\theta} > 45°$, this trend reverses: kink angle decreases with increasing orientation (see bluish curves in larger inset of Fig. 6b).

These findings highlight the intricate, non-monotonic interplay between anisotropy strength and crystal orientation, demonstrating the dominant role of fracture toughness anisotropy in governing the critical crack parameters, even in materials with isotropic elastic stiffness.

3.1.3. *Influence of crystal orientation*

Fig. 7 illustrates the variation of normalized critical energy release rate $\mathcal{G}_c^*/\mathcal{G}_0$ and kink angle θ^* with crystal orientation $\tilde{\theta}$, across various anisotropy strengths $\mathcal{S}$. The analysis below follows the three anisotropy regimes introduced in Section 3.1.2, namely isotropic, lower, and upper anisotropy. The terms “lower" and “upper" reflect the relative positions of the $\mathcal{G}_c^*/\mathcal{G}_0$ vs. $\tilde{\theta}$ and θ^* vs. $\tilde{\theta}$ curves with respect to the isotropic baseline in Fig. 7–lying below and above it, respectively. Notably, the influence of anisotropy strength $\mathcal{S}$ becomes more pronounced as $\mathcal{S}$ deviates further from unity in either direction, indicating a symmetric amplification of anisotropic effects regardless of whether $\mathcal{S} < 1$ or $\mathcal{S} > 1$.

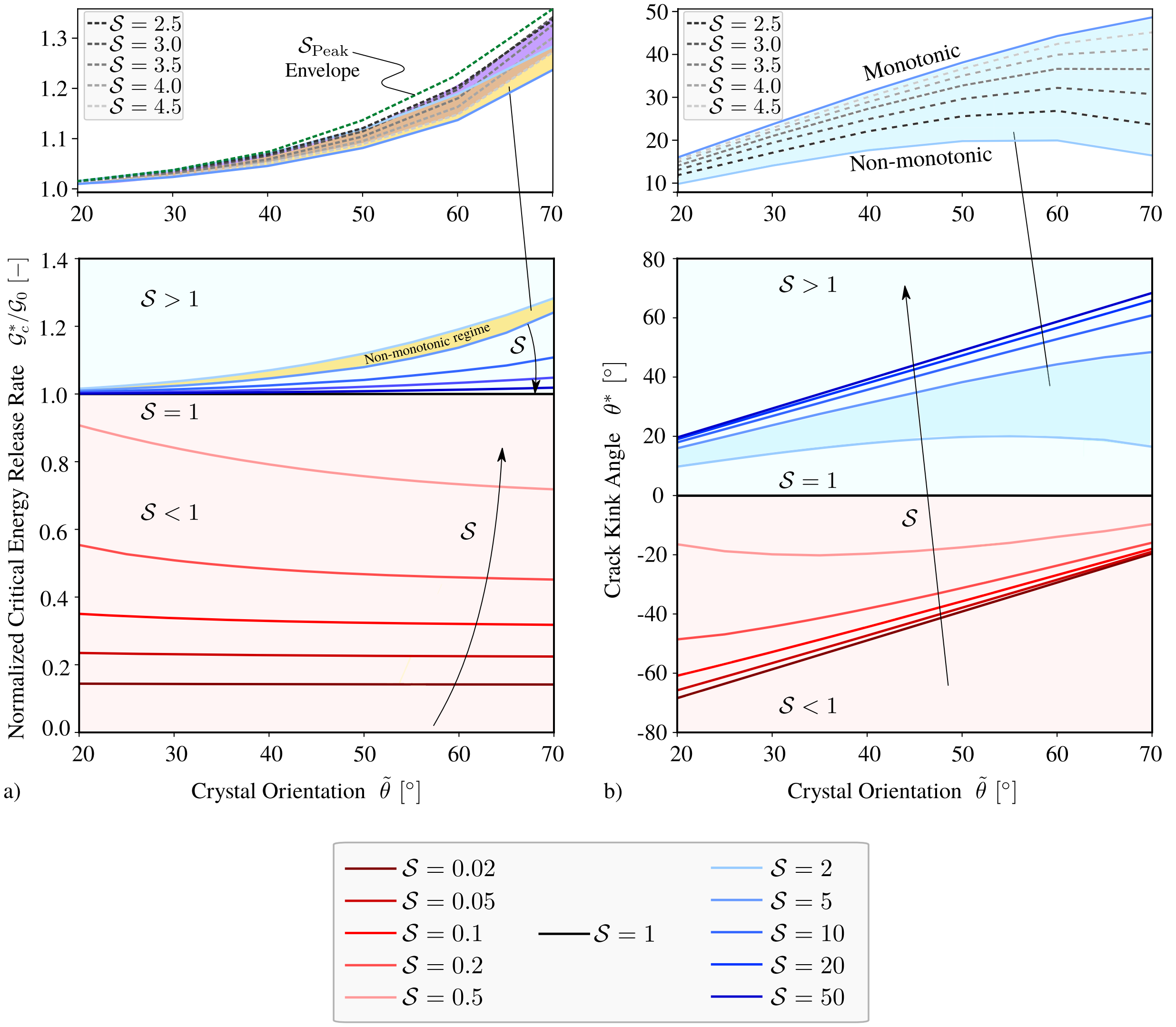

Fig. 7. Plots of a) normalized critical energy release rate $\mathcal{G}_c^*/\mathcal{G}_0$ and b) crack kink angle θ^* as a function of crystal orientation $\tilde{\theta}$, for different values of the anisotropy strength $\mathcal{S}$. Top insets depicting the important regimes showing plots for additional values of $\mathcal{S} \in [2, 5]$.

3.1.3.1. *Implications on Critical Energy Release Rate.*

Fig. 7a shows how the normalized critical energy release rate $\mathcal{G}_c^*/\mathcal{G}_0$ varies with crystal orientation $\tilde{\theta}$ in different regimes:

- *Isotropic Case* ($\mathcal{S} = 1$):
  This case is represented as a horizontal black line in Fig. 7a, where $\mathcal{G}_c^*/\mathcal{G}_0$ remains constant at unity for all orientations.
- *Lower Anisotropy Regime* ($\mathcal{S} < 1$):
  Here, $\mathcal{G}_c^*/\mathcal{G}_0$ decreases monotonically with both increasing $\tilde{\theta}$ and decreasing $\mathcal{S}$, as seen in the red-shaded region of Fig. 7a. For $\mathcal{S} \lesssim 0.1$, $\mathcal{G}_c^*/\mathcal{G}_0$ becomes nearly invariant across $\tilde{\theta}$ (near horizontal darker red curves), due to highly curved Frank plots of the crack resistance (see outer plots in Fig. 5) yielding nearly equidistant tangency points from origin corresponding to $\mathcal{G}_c^*/\mathcal{G}_0$ values, for all orientations.
- *Upper Anisotropy Regime* ($\mathcal{S} > 1$):
  In this regime (blue-shaded region in Fig. 7a), $\mathcal{G}_c^*/\mathcal{G}_0$ increases with orientation, and for fixed $\tilde{\theta}$, follows a non-monotonic trend with $\mathcal{S}$: rising to a peak in the range $\mathcal{S} \in (2, 5)$ before declining toward unity. This behavior is evident in the yellow-shaded region, where each curve attains a maximum at an orientation-dependent peak anisotropy strength, denoted by $\mathcal{S}_{\text{Peak}}$. The upper plot in Fig. 7a highlights this trend for selected values within this interval (shown in purple), while the green envelope marks the bounding behavior associated with $\mathcal{S}_{\text{Peak}}$. Although this envelope theoretically captures the upper bound of $\mathcal{G}_c^*/\mathcal{G}_0$ as a function of orientation, the corresponding $\mathcal{S}_{\text{Peak}}$ values vary with $\tilde{\theta}$, as also illustrated in Fig. 6a. Plots for intermediate $\mathcal{S}$ values in the ranges $(2, \mathcal{S}_{\text{Peak}})$ and $(\mathcal{S}_{\text{Peak}}, 5)$ lie between the respective bounding curves.

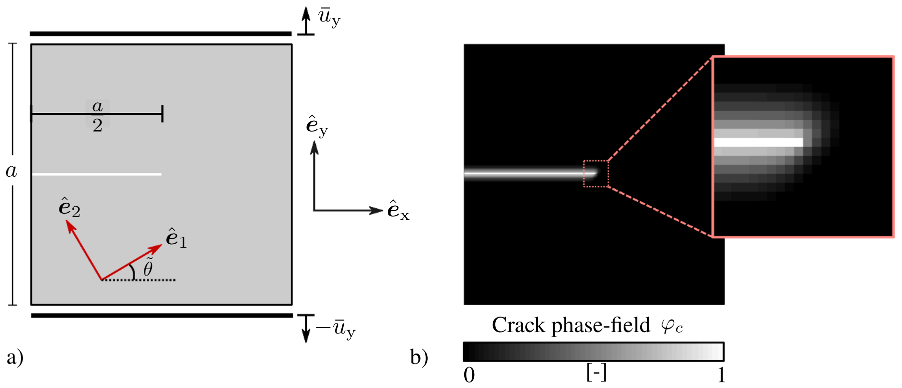

Fig. 8. a) Numerical setup of a square specimen with an initial crack under mode-I loading. Red arrows represent the orthonormal basis $\{\hat{\boldsymbol{e}}_1, \hat{\boldsymbol{e}}_2\}$ of the reference crack surface energy tensor rotated relative to the global basis system $\{\hat{\boldsymbol{e}}_\mathrm{x}, \hat{\boldsymbol{e}}_\mathrm{y}\}$ according to crystal orientation $\tilde{\theta}$. b) Diffuse interface representation of the crack, showing the distribution of the crack phase-field $\varphi_c \in [0, 1]$. The inset highlights the region near the crack tip, where cells exhibit distinct φ_c values.

Implications on Crack Kink Angle. As shown in Fig. 7b, kink angle θ^* is highly sensitive to crystal orientation $\tilde{\theta}$ and anisotropy strength $\mathcal{S}$. For $\mathcal{S} = 1$, kink angles are zero across all orientations. The θ^*-$\tilde{\theta}$ profiles exhibit an anti-symmetry with respect to $\mathcal{S} = 1$. Kink angle increases with $\mathcal{S}$ for fixed orientation, consistent with Fig. 6b. In the parts of upper ($\mathcal{S} \gtrsim 3.7$) and lower ($\mathcal{S} \lesssim 0.28$) anisotropy regimes, kink angle increases monotonically with orientation. In the remaining regions ($0.28 \lesssim \mathcal{S} \lesssim 3.7$) also shown as yellow-shaded region in the inset plot of Fig. 6b, the behavior becomes non-monotonic. For $1 \lesssim \mathcal{S} \lesssim 3.7$, kink angle increases with $\tilde{\theta}$, peaks, then decreases (see inset of Fig. 7b). For $0.28 \lesssim \mathcal{S} \lesssim 1$, the trend reverses – kink angle first decreases, reaches a minimum, then rises again. These non-monotonic patterns underscore the complex, orientation-dependent nature of crack path selection in materials with moderate anisotropy.

3.2. Model validation

For the following numerical examples, a square specimen of edge length a = 100 mm is considered with an initial horizontal crack of length $a/2$ located at mid-height, see Fig. 8a. The specimen is subjected to pure mode-I loading by incrementally applying vertical displacements $\pm\bar{u}_\mathrm{y}$ in steps of $\pm\Delta\bar{u}_\mathrm{y}$ at the top and bottom boundaries, while keeping the lateral edges stress-free. The maximum applied displacements $\pm\bar{u}_\mathrm{y}^\mathrm{max}$ correspond to a total vertical elongation of 1 %, consistent with the small-strain assumption. The reference crack resistance tensor (Eq. (12)) is defined with respect to an orthonormal basis $\{\hat{\boldsymbol{e}}_1, \hat{\boldsymbol{e}}_2\}$, which is rotated by an angle $\tilde{\theta}$ relative to the global coordinate system $\{\hat{\boldsymbol{e}}_\mathrm{x}, \hat{\boldsymbol{e}}_\mathrm{y}\}$. A diffuse initial crack (Fig. 8b) is generated through a preconditioning step, wherein simulation iterations are performed on the given setup without applying any displacements at the boundaries. This numerical setup allows a systematic investigation of the influence of crystal orientation on crack propagation behavior. The mechanical material properties, chosen as representative values for studying crack growth in the small-strain regime, are summarized in Table 1. The chosen simulation parameters are also listed in the same table, unless stated otherwise.

3.2.1. Mesh sensitivity analysis and prediction of critical energy release rate

A mesh sensitivity analysis was performed using the numerical setup in Fig. 8 to evaluate the influence of mesh resolution on model accuracy. Simulations were performed with four mesh sizes $\Delta x \in \{1, 0.5, 0.25, 0.125\}$ at a fixed crystal orientation $\tilde{\theta} = 45°$, for anisotropy strengths $\mathcal{S} \in \{0.1, 1, 10\}$. Figs. 9a,b depict the mean vertical stress $\sigma_\mathrm{yy}^\mathrm{M}$ versus vertical displacement $\bar{u}_\mathrm{y}$ for the isotropic case ($\mathcal{S} = 1$) and an anisotropic case ($\mathcal{S} = 0.1$, $\tilde{\theta} = 45°$). All curves exhibit an initial linear elastic regime, followed by a sudden stress drop marking the onset of crack growth, and subsequent failure at a critical displacement. Finer mesh resolutions lead to earlier crack initiation, as they more accurately capture stress concentrations near the crack tip. The differences in stress-displacement curves diminish for $\Delta x \leq 0.5$ mm, indicating numerical convergence. The simulated critical energy release rate $\mathcal{G}^*_{c,\mathrm{sim}}$ was estimated using the *Displacement Extrapolation Method* (see Section 2.3.2) and compared to the theoretical value $\mathcal{G}^*_c$. The convergence ratio $\mathcal{G}^*_{c,\mathrm{sim}}/\mathcal{G}^*_c$, plotted in Fig. 9c against the resolution $1/\Delta x$, approaches unity with mesh refinement, confirming convergence towards the theoretical value. For the coarsest mesh ($\Delta x = 1$ mm), this ratio ranges from 1.35 to 2.1, indicating overestimation of the critical energy release rate. The lower-row insets showcase the simulated crack kinking patterns at the critical stage, while the upper-row insets display the fully cracked trajectories for different resolutions. The lowest-resolution mesh (Δx =1 mm) exhibits a reduced trajectory tilt, an effect we refer to as *numerical pinning*, which diminishes for finer resolutions.

The accuracy of $\mathcal{G}^*_{c,\mathrm{sim}}$ estimation further improves with finer load step sizes, enabling more precise detection of the critical displacement. Considering both convergence and computational cost, ranging from under 1 CPU-hour for Δx =1 mm to over 5000 CPU-hours at Δx =0.125 mm, a mesh size of Δx =0.5 mm (requiring about 10-20 CPU-hours) was chosen for all subsequent simulations. This resolution offers an optimal trade-off between accuracy and efficiency for predicting crack paths and mechanical responses.

Table 1
Material and simulation parameters used in the study.

Material Parameters			
Parameter	*Symbol*	*Value*	*Unit*
Young's modulus	E	210	GPa
Poisson's ratio	ν	0.3	–
Reference crack resistance	$\mathcal{G}_0$	100	$\mathrm{N\,mm^{-1}}$
Simulation Parameters			
Mesh size	Δx	0.5	mm
Regularization length scale	ϵ	1.5	mm
Displacement step size	$\Delta\bar{u}_{\mathrm{y}}$	0.5	µm
Max. boundary displacement	$\bar{u}_{\mathrm{y}}^{\max}$	0.5	mm
Relaxation parameter	μ	10^{-4}	–
Residual stiffness factor	$\varphi_{\mathrm{residual}}$	10^{-8}	–
Steady-state tolerance	ϵ_{φ_c}	10^{-5}	–
Damage tolerance	$\epsilon_{\mathrm{damage}}$	0.01	–
Simulation Domain Dimensions			
Homogeneous Square Specimen			
Edge length	a	100	mm
Multiphase Rectangular Specimen			
Length	L_{x}	400	mm
Width	L_{y}	200	mm

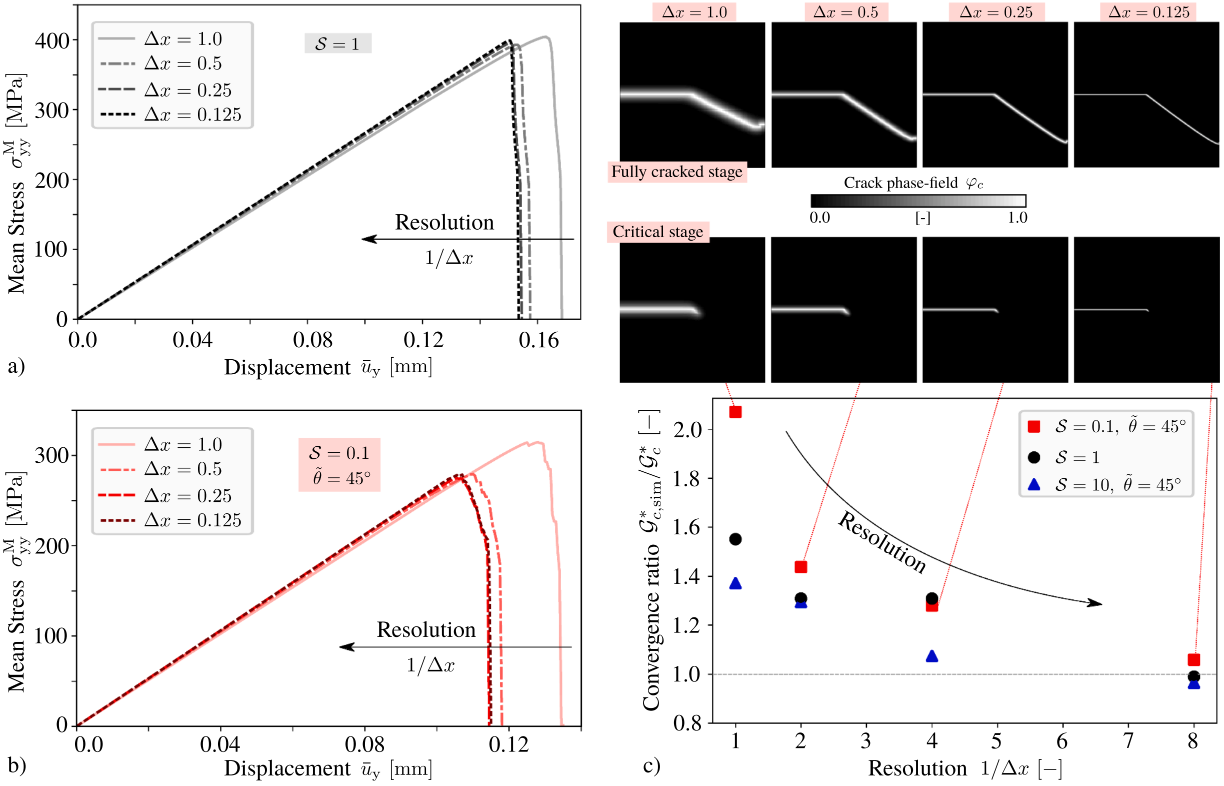

Fig. 9. Plot of the mean vertical stress $\sigma^{\mathrm{M}}_{\mathrm{yy}}$ as a function of imposed vertical displacement $\bar{u}_{\mathrm{y}}$ at the top boundary, for different mesh sizes Δx (or resolutions defined as $1/\Delta x$), for anisotropy strength a) $\mathcal{S} = 1$, and b) $\mathcal{S} = 0.1,\ \tilde{\theta} = 45°$. With increasing resolution, crack initiation occurs at lower critical displacements due to better resolution of stress concentration near the crack tip. c) Plot of convergence ratio, $\mathcal{G}^*_{c,\mathrm{sim}}/\mathcal{G}^*_c$ as a function of resolution $1/\Delta x$, for selected values of anisotropy strength $\mathcal{S}$ and crystal orientation $\tilde{\theta}$. Insets show the simulated crack growth for the case $\mathcal{S} = 0.1,\ \tilde{\theta}$ at the critical (lower row) and fully cracked stage (upper row) for different resolutions. As resolution increases, the convergence ratio approaches unity, indicating convergence of simulation towards the theoretical prediction.

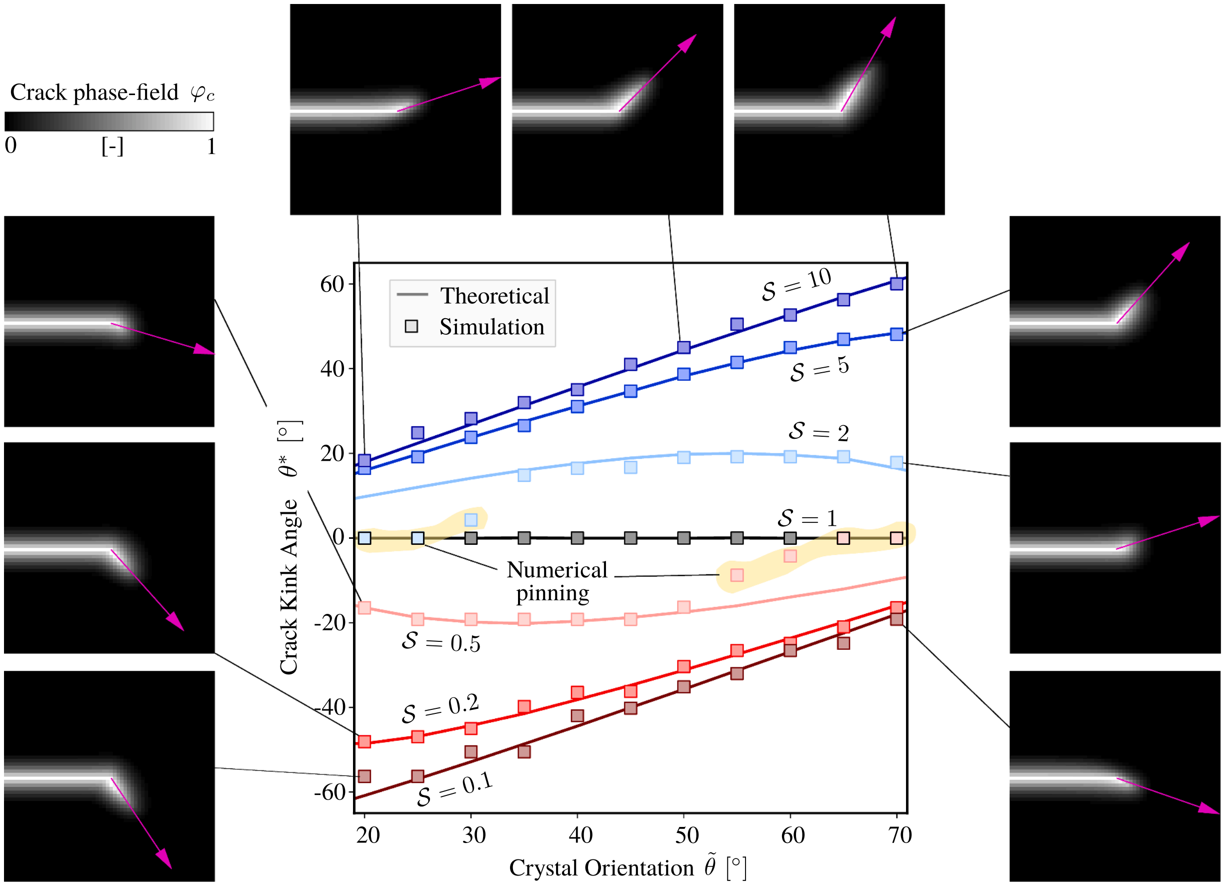

Fig. 10. Plots of crack kink angle θ^* as a function of crystal orientation $\tilde{\theta}$ for various anisotropy strengths $\mathcal{S}$. Solid lines shown in different colors represent the theoretical predictions corresponding to various values of $\mathcal{S}$ indicated in the plot, and discrete points in matching colors denote simulation results. Zoomed insets near crack tip show simulation of crack kinking at the critical stage, with magenta arrows indicating the computed kink angles. Simulated kink angles generally match well with the theoretical values. For anisotropy strengths near unity (i.e. $\mathcal{S} = 0.5, 2$), a numerical pinning effect is observed, resulting in an underestimation of the kink angle magnitude in the yellow-highlighted region, which is expected to diminish with increasing resolution. (For interpretation of the references to colour in this figure legend, the reader is referred to the web version of this article.)

3.2.2. *Prediction of kink angle*

To investigate the influence of anisotropy strength $\mathcal{S}$ and crystal orientation $\tilde{\theta}$ on crack deflection, simulations were performed using a fixed mesh size of $\Delta x = 0.5$. The orientation was varied in the set $\tilde{\theta} \in \{20°, 30°, 40°, 50°, 60°, 70°\}$, and the anisotropy strength in $\mathcal{S} \in \{0.1, 0.2, 0.5, 1, 2, 5, 10\}$, spanning the full range of theoretical kink-angle patterns shown in Fig. 7b. The extreme anisotropy values ($\mathcal{S} = 0.1$ and 10) yield nearly linear and monotonic variations of the kink angle with orientation. Intermediate values ($\mathcal{S} = 0.2$ and 5) show nonlinear yet monotonic trends, while $\mathcal{S} = 0.5$ and 2 exhibit non-monotonic behavior. The isotropic case ($\mathcal{S} = 1$) serves as a baseline, with no crack deflection expected. Kink angles θ^* were extracted from simulations at the critical stage marked by onset of crack growth, identified as the point where the stress-displacement curve begins to decline. The angles were measured using the image processing methodology described in Section 2.3.2. Fig. 10 compares the orientation-dependent kink angle trends obtained from simulations with the corresponding theoretical predictions. The simulated kink angles match well with the theoretical predictions across a broad range of anisotropy strength and crystal orientation. For orientations near the isotropic regime ($\mathcal{S} = 0.5$ and 2), where the magnitude of expected kink angles is small ($|\theta^*| < 20°$), the magnitude of simulated kink angles is underestimated, due to *numerical pinning* (see yellow-shaded region), as previously discussed in Section 3.2.1. These effects reduce with mesh refinement. Overall, the simulations accurately capture the anisotropic trends in kink angle, with deviations typically below 5 %, demonstrating strong quantitative agreement with theoretical relations across a wide range of anisotropy parameters.

3.3. *Anisotropic mechanical response*

For the simulations in Section 3.2.2, the mechanical response is analyzed using mean vertical stress-displacement curves ($\sigma^{\mathrm{M}}_{\mathrm{yy}}$ vs. $\bar{u}_{\mathrm{y}}$) for varying anisotropy strengths $\mathcal{S}$ and crystal orientations $\tilde{\theta}$, as detailed in Sections 3.3.1 and 3.3.2. All cases exhibit an initial

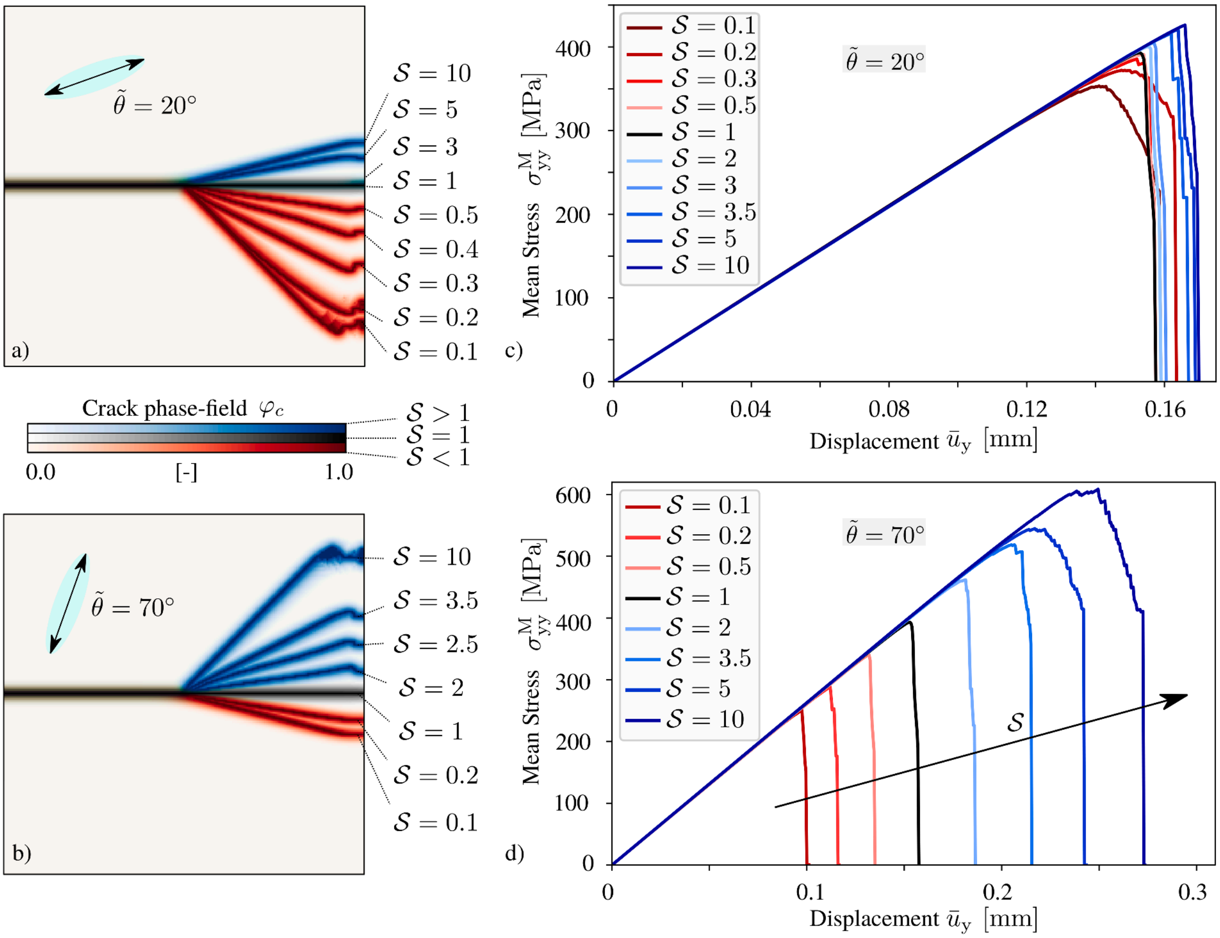

Fig. 11. Simulated crack paths for varying anisotropy strengths $\mathcal{S}$ at crystal orientations (a) $\tilde{\theta} = 20^\circ$ and (b) $\tilde{\theta} = 70^\circ$, lying in the so-called low- and high-orientation regimes, respectively. Crack trajectories are overlaid to enable direct visual comparison. (c-d) Plots of mean vertical stress σ_{yy}^{M} versus vertical displacement $\bar{u}_y$ at the top surface, illustrating the mechanical response for different values of $\mathcal{S}$ at orientations (c) $\tilde{\theta} = 20^\circ$ and (d) $\tilde{\theta} = 70^\circ$.

linear elastic regime, followed by a sudden stress drop upon reaching the critical energy release rate, indicating crack initiation and subsequent growth to complete failure, a characteristic behavior well documented in the literature.

3.3.1. *Influence of anisotropy strength*

Fig. 11 shows the effect of anisotropy strength $\mathcal{S}$ on crack trajectories and mechanical response curves for two representative crystal orientations: $\tilde{\theta} = 20^\circ$ and 70°, corresponding to the *low-* and *high-orientation regimes*. These cases mark the limits of the studied orientation range, with trends qualitatively extending to nearby orientations. The discussion is organized accordingly in Figs. 11a,c (low-orientation) and 11b,d (high-orientation). Across both regimes, distinct deflection patterns emerge. For $\mathcal{S} > 1$, cracks consistently deflect toward the crystal orientation, with alignment increasing as $\mathcal{S}$ increases, as seen in the blue contours of the crack phase-field φ_c. Conversely, for $\mathcal{S} < 1$, cracks deflect away from the crystal orientation (red φ_c contours), tilting toward orthogonal directions, with deflection becoming more pronounced as $\mathcal{S}$ decreases. These trends highlight how anisotropic fracture surface energy guides crack propagation along energetically favorable directions, governed by the strength of anisotropy.

Fig. 11c,d presents the mechanical responses corresponding to the simulated crack paths. A general trend across both orientation regimes is evident: larger crack deflections (typically exceeding 45°) lead to a more gradual stress drop during the critical stage, reflecting increased geometric resistance due to the tilted crack path. In contrast, cracks that remain closer to the initial horizontal direction show a sharp stress drop at a distinct critical displacement, indicating crack growth with lower geometric impediment. These contrasting responses highlight the interplay between crack deflection and fracture resistance. For clarity, the mechanical behavior is further examined separately for each orientation regime in the following sections.

3.3.1.1. Low-Orientation Regime ($\tilde{\theta} = 20^\circ$). The corresponding mechanical responses, shown in Fig. 11c, exhibit a drop in mean vertical stress within a narrow critical displacement range, $\bar{u}_y \in (0.15, 0.17)$ mm. For $\mathcal{S} \geq 1$, a clear trend emerges: increasing anisotropy

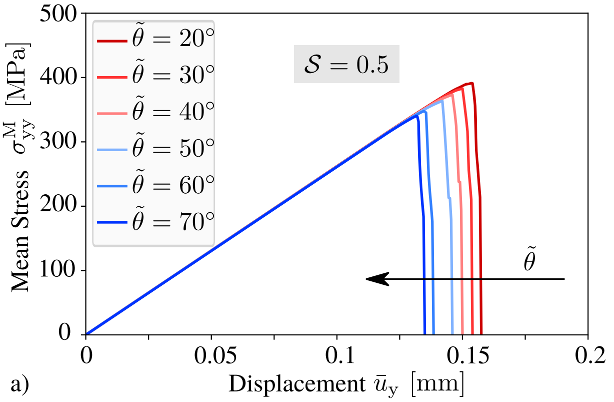

Fig. 12. Plots of mean vertical stress $\sigma^{\mathrm{M}}_{\mathrm{yy}}$ versus imposed vertical displacement $\bar{u}_{\mathrm{y}}$ on the top surface for different values of crystal orientation $\tilde{\theta}$ for anisotropy strengths a) $\mathcal{S} = 0.5$ and b) $\mathcal{S} = 2$.

strength (bluish curves) systematically shifts the critical displacement to higher values, indicating enhanced resistance to crack initiation. In contrast, for $\mathcal{S} < 1$, the response curves (reddish tones) show no systematic pattern in peak stress or critical displacement, revealing a more complex interplay of fracture parameters. This behavior is elucidated by examining the joint influence of the (normalized) critical energy release rate $\mathcal{G}_c^*/\mathcal{G}_0$ and the kink angle θ^* with orientation $\tilde{\theta}$, see Fig. 7. For $\mathcal{S} > 1$ at $\tilde{\theta} = 20°$, $\mathcal{G}_c^*/\mathcal{G}_0$ remains close to the isotropic baseline of unity, varying only slightly with $\mathcal{S}$. However, the kink angle increases significantly with $\mathcal{S}$, introducing additional geometric resistance of deflecting the crack. Their combined effect results in delayed onset of fracture growth at higher critical displacements $\bar{u}_{\mathrm{y}}$, as reflected in the blue response curves in Fig. 11c. For $\mathcal{S} < 1$, the situation becomes more intricate. Although $\mathcal{G}_c^*/\mathcal{G}_0$ decreases with decreasing $\mathcal{S}$ (Fig. 7a), which would typically imply crack initiation at lower $\bar{u}_{\mathrm{y}}$-values, the simultaneous increase in the kink angle magnitude introduces a competing geometric resistance that counteracts this effect. These opposing effects largely balance each other, resulting in mechanical responses (red curves) that remain close to the isotropic baseline. This subtle interplay highlights the nuanced coupling between fracture energetics and crack deflection, particularly in low-orientation regime.

3.3.1.2. High-Orientation Regime ($\tilde{\theta} = 70°$). In this regime, the mechanical response curves (Fig. 11d) exhibit a distinct and systematic trend: the critical displacement $\bar{u}_{\mathrm{y}}$ increases monotonically with increasing anisotropy strength $\mathcal{S}$. This hardening behavior is particularly notable given the non-monotonic variation in the (normalized) critical energy release rate $\mathcal{G}_c^*/\mathcal{G}_0$ with $\mathcal{S}$ (Fig. 6a), especially within the intermediate range $\mathcal{S} \in (2, 5)$, where $\mathcal{G}_c^*/\mathcal{G}_0$ reaches a peak value at a given $\mathcal{S}_{\mathrm{Peak}}$, see Section 3.1.2. The resolution to this apparent contradiction lies again in the interplay between critical energy release rate and kink angle. At crystal orientation $\tilde{\theta} = 70°$, although $\mathcal{G}_c^*/\mathcal{G}_0$ decreases in the range $\mathcal{S} \in (\mathcal{S}_{\mathrm{Peak}}, 50)$, see Fig. 7a, the kink angle θ^* continues to increase monotonically (blue-shaded region in Fig. 7b). This enhanced deflection contributes significant geometric resistance, effectively raising the barrier to crack propagation despite a lower intrinsic crack resistance. Consequently, the critical displacement $\bar{u}_{\mathrm{y}}$ shifts to higher values with increasing $\mathcal{S}$. These results emphasize the dominant role of crack path geometry in governing fracture initiation in high orientation regime, even when the critical energy release rate decreases.

3.3.2. Influence of crystal orientation

Fig. 12 depicts the mechanical response as a function of crystal orientation $\tilde{\theta}$ for the anisotropy strength of $\mathcal{S} = 0.5$ and $\mathcal{S} = 2$, belonging to the lower ($\mathcal{S} < 1$) and upper anisotropy ($\mathcal{S} > 1$) regimes, respectively. A clear contrast emerges between the two regimes. In the lower anisotropy case ($\mathcal{S} = 0.5$), the critical displacement $\bar{u}_{\mathrm{y}}$ (marked by drop in vertical stress) systematically decreases with increasing crystal orientation from 20° to 70° (Fig. 12a). This trend reflects a softening mechanical response at higher orientations. In contrast, the upper anisotropy case ($\mathcal{S} = 2$) exhibits a hardening behavior, with increasing critical displacements required for crack initiation as $\tilde{\theta}$ increases (Fig. 12b). This reversal in trend between the two regimes can be explained by examining the variation of the normalized critical energy release rate $\mathcal{G}_c^*/\mathcal{G}_0$ and the kink angle θ^* with orientation $\tilde{\theta}$, as shown in Fig. 7. For $\mathcal{S} = 0.5$, $\mathcal{G}_c^*/\mathcal{G}_0$ decreases with increasing orientation, indicating a reduced critical energy release rate at higher $\tilde{\theta}$. Conversely, for $\mathcal{S} = 2$, $\mathcal{G}_c^*/\mathcal{G}_0$ increases with $\tilde{\theta}$, implying enhanced critical energy release rate at higher orientations. Although the kink angle θ^* exhibits a non-monotonic dependence on $\tilde{\theta}$ in both cases, the difference in magnitudes remains small (typically below 10°). As a result, the influence of kink angle on the mechanical response is secondary to that of the critical energy release rate, whose steeper and monotonic variation predominantly governs the observed trends in mechanical response for both the cases.

3.4. Consistent vs. classical anisotropy formulation: a comparative analysis

Finally, we compare the performance of the proposed consistent anisotropy formulation with the widely adopted classical anisotropy formulation, discussed in Section 2.1.1.1. A detailed comparison is presented in Section 3.4.1, where crack propagation is simulated in a homogeneous single-phase solid under mode-I loading. Both formulations are evaluated based on the resulting

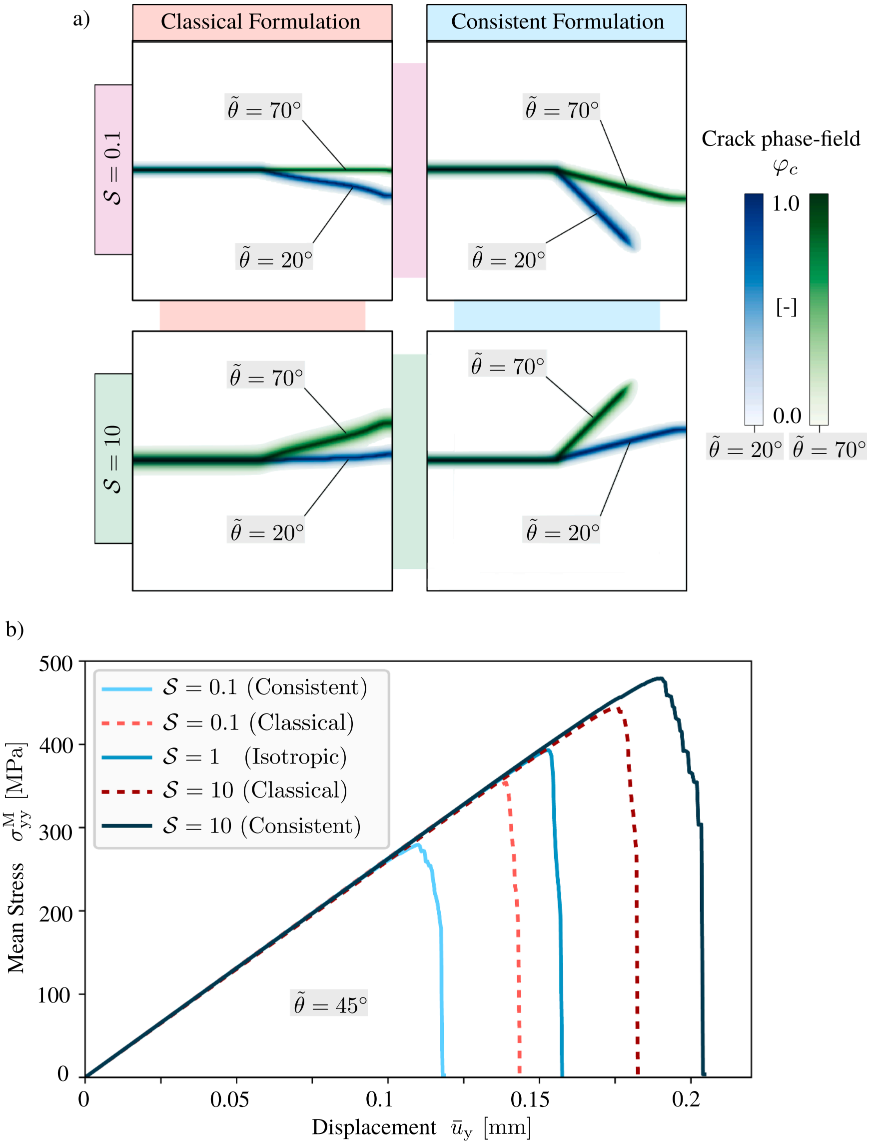

Fig. 13. a) Simulated crack paths in a single-phase solid under mode-I loading for crystal orientations $\tilde{\theta} = 20°$ and 70°, comparing the classical and consistent anisotropy formulations at anisotropy strengths $\mathcal{S} = 0.1$ and 10. Overlayed images highlight differences in crack deflection behavior. b) Mean vertical stress σ_{yy}^{M} versus imposed vertical displacement $\bar{u}_y$ at the top surface, comparing the mechanical response of the two formulations for varying anisotropy strengths $\mathcal{S} \in \{0.1, 1, 10\}$ at a fixed crystal orientation $\tilde{\theta} = 45°$.

crack paths and their mechanical responses. This comparative analysis is further extended in Section 3.4.2 to multiphase materials, allowing us to assess the influence of anisotropy formulation on crack behavior in structurally heterogeneous solids.

3.4.1. *Crack growth in single-phase solids*

Using the numerical setup and boundary conditions detailed in Section 3.2 and illustrated in Fig. 8, we compare the predicted crack paths and mechanical responses of the proposed *consistent anisotropy formulation* with those of the commonly used *classical* formulation.

3.4.1.1. Implications on Crack Paths. Fig. 13a compares the simulated crack trajectories for representative cases with crystal orientations $\tilde{\theta} = 20°$ and 70°, and anisotropy strengths $\mathcal{S} = 0.1$ and 10, using both the consistent and classical formulations. In classical formulation, the crack deflection is systematically underestimated, along the crystal orientation for $\mathcal{S} = 10$, and in the orthogonal direction for $\mathcal{S} = 0.1$. This is due to the partially isotropic treatment of the crack surface energy, which weakens anisotropy and introduces orientation-dependent variations in the interface width, as discussed in Section 2.1.1. In contrast, the consistent formulation fully incorporates anisotropy in the surface energy, yielding uniform interface widths and kink angles closely matching theoretical

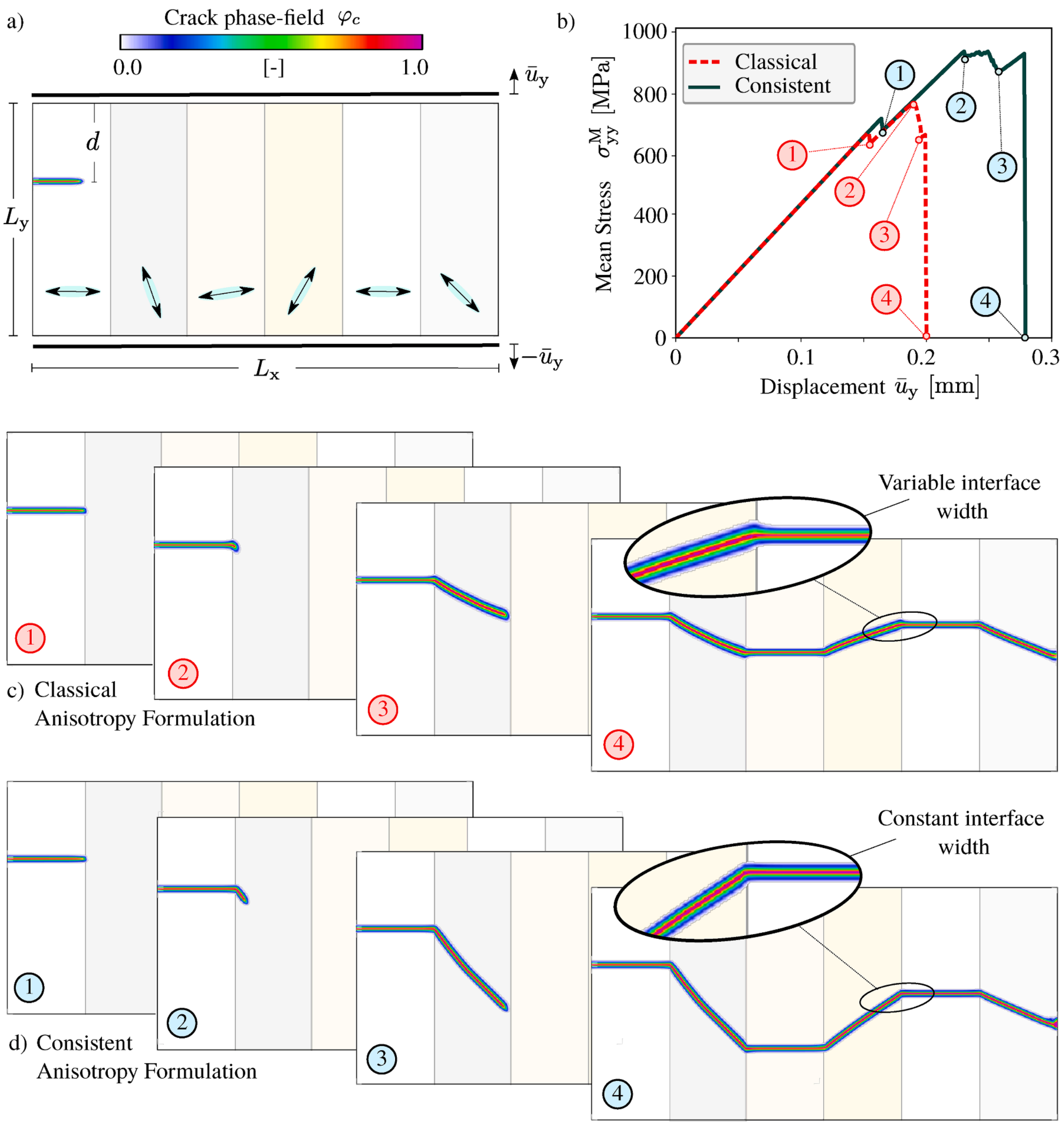

Fig. 14. (a) Numerical setup of a rectangular multiphase specimen with dimensions $L_x = 400\,\text{mm} \times L_y = 200\,\text{mm}$, composed of horizontally stacked phases and containing an initial horizontal diffuse crack of length 40 mm at a vertical distance $d = 66\,\text{mm}$, subjected to mode-I loading. The crack phase-field φ_c is shown as a contour plot. Arrows indicate the crystal orientations of each phase, corresponding to directions of lowest crack resistance. (b) Mean vertical stress σ^M_{yy} versus imposed vertical displacement $\bar{u}_y$ on the top surface, comparing the material response of the classical and consistent models. (c-d) Simulated crack paths at selected stages for (c) the classical model and (d) the consistent model. The classical model exhibits variable interface widths across phases, while the consistent model maintains a constant interface width. The two models exhibit different crack paths and overall material responses.

predictions. Consequently, it delivers accurate and physically consistent crack deflection behavior across both weakly and strongly anisotropic regimes.

3.4.1.2. Implications on Mechanical Response. Fig. 13b presents the mechanical response for varying anisotropy strengths $\mathcal{S} \in \{0.1, 1, 10\}$ at a fixed crystal orientation of $\tilde{\theta} = 45°$, comparing the consistent and classical formulations. For $\mathcal{S} = 1$, both formulations reduce to the isotropic case, producing identical horizontal crack paths and mechanical behavior. However, at $\mathcal{S} = 0.1$ and 10, clear discrepancies emerge due to the differing treatments of anisotropy. At $\mathcal{S} = 0.1$, the consistent formulation predicts a softer response, characterized by a lower critical displacement $\bar{u}_y$, relative to the classical model. Conversely, for $\mathcal{S} = 10$, the classical formulation exhibits a softer response. This reversal is attributed to the isotropic potential contribution retained in the classical formulation, which moderates the anisotropic effect. Consequently, its predicted mechanical response consistently falls between that of the fully anisotropic consistent model and the isotropic baseline across both ends of the anisotropy spectrum.

3.4.2. Crack growth in multiphase solids

Fig. 14a depicts a rectangular multiphase specimen of dimensions $L_\mathrm{x} = 400\,\mathrm{mm} \times L_\mathrm{y} = 200\,\mathrm{mm}$, composed of horizontally stacked solid phases. An initial horizontal diffuse crack of length $40\,\mathrm{mm}$ is located $d = 66\,\mathrm{mm}$ below the top boundary. Mode-I loading is applied through incremental vertical displacements $\bar{u}_\mathrm{y}$ and $-\bar{u}_\mathrm{y}$ at the top and bottom surfaces, while the lateral boundaries are kept stress-free. Each phase is assigned an anisotropy strength of $\mathcal{S} = 10$, with differing crystallographic orientations indicated by arrows. The mechanical and simulation parameters used are listed in Table 1. For this setup, the Voigt/Taylor homogenization scheme used in the present work is equivalent to the mechanical jump conditions at the interface, enabling accurate calculation of stresses and strains in the diffuse solid-solid interfacial region. Crack growth simulations were performed using both the consistent and classical anisotropy formulations. The resulting mechanical responses are shown in Fig. 14b, plotted as the mean vertical stress $\sigma^\mathrm{M}_\mathrm{yy}$ versus the applied displacement $\bar{u}_\mathrm{y}$. Snapshots of crack evolution at different loading stages are presented in Figs. 14c, d. As established in the single-phase simulations (Section 3.4.1), the classical formulation systematically underestimates crack deflection in each phase. Furthermore, it introduces a modeling artifact in the form of phase- and orientation-dependent interface widths (see insets of Figs. 14c,d), due to the partial incorporation of anisotropy in the crack surface energy. In contrast, the proposed consistent formulation fully integrates anisotropy in both the regularization terms of crack surface energy, thereby eliminating these spurious width variations, resulting in more accurate crack trajectories and a mechanical response that better captures the correct energetics and interfacial behavior. The mechanical response predicted by the consistent formulation is notably stiffer throughout all loading stages, see Fig. 14b. The onset of crack growth is marked by the first peak, where the crack begins to grows and reaches the first phase boundary at stage 1. At this point, the consistent formulation predicts a higher critical displacement, in agreement with the trend observed in homogeneous specimens for $\mathcal{S} > 1$ in Fig. 13b.

Subsequent stages highlight the crack's interaction with different phases. At stage 2, the crack enters the second phase after crossing a higher energy barrier at the first grain boundary. This transition is accompanied by a larger stress peak, attributed to the greater misorientation of the second phase, which results in a stiffer mechanical response, as expected in the regime $\mathcal{S} > 1$ (Fig. 12b). The stress then decreases until stage 3, signaling crack propagation within the second phase. Owing to the increased misorientation in this phase, the consistent model again predicts a higher critical displacement and a more pronounced crack deflection. This manifests as a gradual stress decline, a trend also observed in earlier single-phase simulations. Upon reaching the second interphase boundary, the crack encounters another energy barrier before progressing toward complete failure (at stage 4) in both models. The final critical displacement remains higher for the consistent formulation, as anticipated.

4. Conclusion and outlook

This work presents a physically consistent formulation of anisotropy in crack surface energy within the phase-field modeling framework, enabling a quantitative treatment of direction-dependent fracture in multiphase materials. At its core, the present work links anisotropy parameters to critical fracture properties through an iterative graphical method based on the classical Generalized Maximum Energy Release Rate (GMERR) criterion. These theoretical relations uncover a rich, non-monotonic interplay between crack kinking angles and energy release rates, shedding light on the intricate mechanics of fracture in anisotropic solids. Validation through benchmark simulations confirms quantitative agreement with theory across a broad range of anisotropy parameters. Numerical crack pinning emerges in low-anisotropy cases but diminishes with mesh refinement, affirming the numerical robustness of the formulation. The simulated mechanical responses reveal how anisotropy-driven variations in kink angles and fracture toughness govern whether materials exhibits softening or stiffening during crack growth, providing a clear physical interpretation through the lens of the derived relations. A critical comparison with the widely used classical anisotropy model, where only the gradient term is treated as anisotropic, highlights the necessity of a consistent formulation. The classical model introduces orientation-dependent interface widths and systematically underestimates crack deflections, leading to weakened anisotropic fracture responses. In contrast, the proposed model ensures accurate crack paths and uniform interface widths by treating both gradient and potential terms coherently. These advantages extend seamlessly to multiphase systems, where consistent anisotropy ensures a uniform interface width across distinct phases and orientations, crucial for quantitative modeling of failure in real-world polycrystalline and composite materials. By unifying numerical implementation with theoretical principles, the present work enhances both the fidelity and understanding of phase-field fracture simulations in anisotropic media.

The way forward is replete with possibilities. While this work focuses on two-dimensional simulations, the extension to three dimensions is straightforward and promises broader applicability. For poly-crystals with arbitrarily oriented grain boundaries, the model must be extended with the generalized mechanical jump conditions [54,69,70]. For strongly heterogeneous materials, the multiple crack order parameter approach of Schöller et al. [57] offers a natural extension. The current validation workflow, deriving and testing theoretical predictions, can accommodate arbitrary anisotropy functions within the convex (weakly anisotropic) regime. In the case of strongly anisotropic surface energies, which require higher-order regularization, this work provides the groundwork for a consistent formulation, addressing key limitations of current models that treat anisotropy only partially.

CRediT authorship contribution statement

Nishant Prajapati: Writing – review & editing, Writing – original draft, Visualization, Validation, Software, Methodology, Investigation, Formal analysis, Conceptualization; **Lukas Schöller:** Writing – review & editing, Software, Methodology, Conceptualization; **Martin Reder:** Writing – review & editing, Software, Conceptualization; **Daniel Schneider:** Writing – review & editing, Supervision, Methodology, Conceptualization; **Britta Nestler:** Writing – review & editing, Resources, Project administration, Methodology, Funding acquisition.

Declaration of Generative AI and AI-assisted Technologies in the Writing Process

During the preparation of this work the author(s) used ChatGPT in order to improve the readability and language of the manuscript. After using this tool/service, the author(s) reviewed and edited the content as needed and take(s) full responsibility for the content of the published article.

Data availability

The simulation model described in this article was implemented in the in-house multiphysics software framework PACE3D. A software license can be obtained through the Steinbeis Network (www.steinbeis.de) under the management of Prof. Dr. Britta Nestler and Dr.-Ing. Michael Selzer, within the subject area *Material Simulation and Process Optimization*. Theoretical results can be reproduced based on the methodologies detailed in the article, and the corresponding data can be made available upon request. Simulation results are reproducible using the provided parameters in combination with PACE3D.

Declaration of competing interest

The authors declare that they have no known competing financial interests or personal relationships that could have appeared to influence the work reported in this paper.

Acknowledgements

The authors acknowledge funding of this research by the Helmholtz Association under the program MTET (no. 38.04.04). LS gratefully acknowledges support from the D-A-CH project titled “Ceria-based Cathodes for High-Performance Electrolysis Cells” and the DFG grant number 467256728.

Appendix A. Anisotropic Crack Resistance

In 2D, the analytical expression for the *Root-Squared-Orthotropic* crack resistance anisotropy function (Eq. (10)) is given by

$$\begin{aligned}\mathcal{G}_c(\theta;\tilde{\theta}) &= \mathcal{G}_c\left(\boldsymbol{n}_c(\theta);\tilde{\theta}\right)\\ &= \sqrt{\boldsymbol{\mathcal{G}}_c^2\left(\boldsymbol{\mathcal{G}}_{c_0},\tilde{\theta}\right) : \left(\boldsymbol{n}_c(\theta)\otimes\boldsymbol{n}_c(\theta)\right)}\\ &= \sqrt{\boldsymbol{Q}(\tilde{\theta})\,\boldsymbol{\mathcal{G}}_{c_0}^2\,\boldsymbol{Q}^T(\tilde{\theta}) : \left(\boldsymbol{n}_c(\theta)\otimes\boldsymbol{n}_c(\theta)\right)}\\ &= \sqrt{\mathcal{G}_{c_0 1}^2\sin^2\left(\theta-\tilde{\theta}\right)+\mathcal{G}_{c_0 2}^2\cos^2\left(\theta-\tilde{\theta}\right)}\end{aligned} \tag{A.1}$$

in terms of the unit normal vector $\boldsymbol{n}_c$ to the crack surface, reference crack resistance tensor $\boldsymbol{\mathcal{G}}_{c_0}$ and rotation tensor $\boldsymbol{Q}$, given by:

$$\boldsymbol{n}_c(\theta) = \begin{pmatrix}-\sin\theta\\ \cos\theta\end{pmatrix},\quad \boldsymbol{\mathcal{G}}_{c_0} = \begin{pmatrix}\mathcal{G}_{c_0 1} & 0\\ 0 & \mathcal{G}_{c_0 2}\end{pmatrix},\quad \boldsymbol{Q}(\tilde{\theta}) = \begin{pmatrix}\cos\tilde{\theta} & -\sin\tilde{\theta}\\ \sin\tilde{\theta} & \cos\tilde{\theta}\end{pmatrix}, \tag{A.2}$$

parameterized using the polar angle θ defined between the crack tangent and the global x-axis, and crystal orientation $\tilde{\theta}$ relative to the global frame. The anisotropy arises from differences between the components $\mathcal{G}_{c_0 1}$ and $\mathcal{G}_{c_0 2}$ of the reference crack resistance tensor.

Appendix B. Energy release rate

Following Amestoy and Leblond [67], the energy release rate (Eq. (22)) in Section 2.2.2 is expressed in terms of effective stress intensity factors $\tilde{K_I}$ and $\tilde{K_{II}}$, given as linear combinations of the mode I and II factors, K_I and K_{II}:

$$\tilde{K_I} = F_{11}K_I + F_{12}K_{II}, \quad \tilde{K_{II}} = F_{21}K_I + F_{22}K_{II}. \tag{B.1}$$

The coefficients F_{ij} for $i,j\in\{1,2\}$ are universal functions of the kink angle θ, approximated by a 20th-degree power series:

$$F_{11} = 1 - \frac{3\pi^2}{8}m^2 + \left(\pi^2 - \frac{5\pi^4}{128}\right)m^4 + \left(\frac{\pi^2}{9} - \frac{11\pi^4}{72} + \frac{119\pi^6}{15360}\right)m^6 + 5.0779m^8$$

$$\begin{aligned}
&-2.88312m^{10}-0.0925m^{12}+2.996m^{14}-4.059m^{16}+1.63m^{18}+4.1m^{20},\\
F_{12}&=-\frac{3\pi}{2}m+\left(\frac{10\pi}{3}+\frac{\pi^3}{16}\right)m^3-\left(2\pi+\frac{133\pi^3}{180}-\frac{59\pi^5}{1280}\right)m^5+12.313906\,m^7\\
&-7.32433m^9+1.5793m^{11}+4.0216m^{13}-6.915m^{15}+4.21m^{17}+4.56m^{19},\\
F_{21}&=\frac{\pi}{2}m-\left(\frac{4\pi}{3}+\frac{\pi^3}{48}\right)m^3-\left(\frac{2\pi}{3}-\frac{13\pi^3}{30}+\frac{59\pi^5}{3840}\right)m^5-6.176023m^7\\
&+4.44112m^9-1.534m^{11}-2.07m^{13}+4.684m^{15}-3.95m^{17}-1.32m^{19},\\
F_{22}&=1-\left(4+\frac{3\pi^2}{8}\right)m^2+\left(\frac{8}{3}+\frac{29\pi^2}{18}-\frac{5\pi^4}{128}\right)m^4\\
&-\left(\frac{32}{15}+\frac{4\pi^2}{9}+\frac{1159\pi^4}{7200}-\frac{119\pi^6}{15360}\right)m^6+10.58254m^8-4.78511m^{10}\\
&-1.8804m^{12}+7.28m^{14}-7.591m^{16}+0.25m^{18}+12.5m^{20},
\end{aligned} \tag{B.2}$$

with $m=\theta/\pi$ $(-1<m<+1)$.

Appendix C. Displacement Extrapolation Method

According to linear elastic fracture mechanics [71], the crack opening displacement (COD) Δu_{y} near the crack tip along the crack plane $(\theta=\pi)$ is given by:

$$\Delta u_{\mathrm{y}}(r,\theta=\pi)=\frac{4K_I(1-\nu^2)}{E}\sqrt{\frac{r}{2\pi}}, \tag{C.1}$$

where K_I is the mode I stress intensity factor, E is Young's modulus, ν is Poisson's ratio, and r is the distance from the crack tip. Fitting Δu_{y} vs. $\sqrt{r}$ yields a slope m, from which K_I is computed as:

$$K_I=\frac{m}{\frac{4(1-\nu^2)}{E}\sqrt{\frac{1}{2\pi}}}. \tag{C.2}$$

At critical loading, Eq. (C.2) yields K_{Ic}, and the corresponding critical energy release rate reads:

$$\mathcal{G}_c^*=\frac{K_{Ic}^2(1-\nu^2)}{E}. \tag{C.3}$$

For details, see e.g. Zhu and Oterkus [68].

References

[1] A.A. Griffith, VI. The phenomena of rupture and flow in solids, Philos. Trans. R. Soc. Lond. Ser. A, Contain. Pap. Math. Phys. Character 221 (582–593) (1921) 163–198.

[2] G.A. Francfort, J.-J. Marigo, Revisiting brittle fracture as an energy minimization problem, J. Mech. Phys. Solids 46 (8) (1998) 1319–1342.

[3] B. Bourdin, G.A. Francfort, J.-J. Marigo, The variational approach to fracture, J. Elast. 91 (1) (2008) 5–148.

[4] C. Kuhn, R. Müller, A continuum phase field model for fracture, Eng. Fract. Mech. 77 (18) (2010) 3625–3634.

[5] L.O. Eastgate, J.P. Sethna, M. Rauscher, T. Cretegny, C.-S. Chen, C.R. Myers, Fracture in mode i using a conserved phase-field model, Phys. Rev. E 65 (3) (2002) 036117.

[6] R. Spatschek, M. Hartmann, E. Brener, H. Müller-Krumbhaar, K. Kassner, Phase field modeling of fast crack propagation, Phys. Rev. Lett. 96 (1) (2006) 015502.

[7] C. Miehe, F. Welschinger, M. Hofacker, Thermodynamically consistent phase-field models of fracture: variational principles and multi-field FE implementations, Int. J. Numer. Methods Eng. 83 (10) (2010) 1273–1311.

[8] M.J. Borden, C.V. Verhoosel, M.A. Scott, T.J.R. Hughes, C.M. Landis, A phase-field description of dynamic brittle fracture, Comput. Methods Appl. Mech. Eng. 217 (2012) 77–95.

[9] M. Ambati, T. Gerasimov, L. De Lorenzis, Phase-field modeling of ductile fracture, Comput. Mech. 55 (5) (2015) 1017–1040.

[10] M. Ambati, T. Gerasimov, L. De Lorenzis, A review on phase-field models of brittle fracture and a new fast hybrid formulation, Comput. Mech. 55 (2) (2015) 383–405.

[11] E.C. Bryant, W. Sun, A mixed-mode phase field fracture model in anisotropic rocks with consistent kinematics, Comput. Methods Appl. Mech. Eng. 342 (2018) 561–584.

[12] A. Mesgarnejad, A. Imanian, A. Karma, Phase-field models for fatigue crack growth, Theor. Appl. Fract. Mech. 103 (2019) 102282.

[13] R. Kobayashi, Modeling and numerical simulations of dendritic crystal growth, Physica D 63 (3–4) (1993) 410–423.

[14] J.D. Clayton, J. Knap, A geometrically nonlinear phase field theory of brittle fracture, Int. J. Fract. 189 (2) (2014) 139–148.

[15] J.D. Clayton, J. Knap, Phase field modeling of directional fracture in anisotropic polycrystals, Comput. Mater. Sci. 98 (2015) 158–169.

[16] J.D. Clayton, J. Knap, Phase field modeling and simulation of coupled fracture and twinning in single crystals and polycrystals, Comput. Methods Appl. Mech. Eng. 312 (2016) 447–467.

[17] B. Li, C. Peco, D. Millán, I. Arias, M. Arroyo, Phase-field modeling and simulation of fracture in brittle materials with strongly anisotropic surface energy, Int. J. Numer. Methods Eng. 102 (3–4) (2015) 711–727.

[18] S. Teichtmeister, D. Kienle, F. Aldakheel, M.A. Keip, Phase field modeling of fracture in anisotropic brittle solids, Int. J. Non Linear Mech. 97 (2017) 1–21.

[19] N. Nguyen-Thanh, W. Li, J. Huang, K. Zhou, Adaptive higher-order phase-field modeling of anisotropic brittle fracture in 3D polycrystalline materials, Comput. Methods Appl. Mech. Eng. 372 (2020) 113434.

[20] S. Nagaraja, U. Römer, H.G. Matthies, L. De Lorenzis, Deterministic and stochastic phase-field modeling of anisotropic brittle fracture, Comput. Methods Appl. Mech. Eng. 408 (2023) 115960.

[21] R. Ma, W. Sun, FFT-Based solver for higher-order and multi-phase-field fracture models applied to strongly anisotropic brittle materials, Comput. Methods Appl. Mech. Eng. 362 (2020) 112781.

[22] Z. Luo, L. Chen, N. Wang, B. Li, A phase-field fracture model for brittle anisotropic materials, Comput. Mech. 70 (5) (2022) 931–943.
[23] A. Takei, B. Roman, J. Bico, E. Hamm, F. Melo, Forbidden directions for the fracture of thin anisotropic sheets: an analogy with the wulff plot, Phys. Rev. Lett. 110 (14) (2013) 144301.
[24] N. Noii, M. Fan, T. Wick, Y. Jin, A quasi-monolithic phase-field description for orthotropic anisotropic fracture with adaptive mesh refinement and primal–dual active set method, Eng. Fract. Mech. 258 (2021) 108060.
[25] T.-T. Nguyen, J. Réthoré, J. Yvonnet, M.-C. Baietto, Multi-phase-field modeling of anisotropic crack propagation for polycrystalline materials, Comput. Mech. 60 (2017) 289–314.
[26] Z. Liu, D. Juhre, Phase-field modelling of crack propagation in anisotropic polycrystalline materials, Procedia Struct. Integrity 13 (2018) 787–792.
[27] X. Hu, X. Gong, N. Xie, Q. Zhu, P. Guo, H. Hu, J. Ma, Modeling crack propagation in heterogeneous granite using grain-based phase field method, Theor. Appl. Fract. Mech. 117 (2022) 103203.
[28] N. Ma, Q. Chen, Y. Wang, Implementation of high interfacial energy anisotropy in phase field simulations, Scr. Mater. 54 (11) (2006) 1919–1924.
[29] S. Torabi, J. Lowengrub, A. Voigt, S. Wise, A new phase-field model for strongly anisotropic systems, Proc. R. Soc. A: Math., Phys. Eng. Sci. 465 (2105) (2009) 1337–1359.
[30] I. Steinbach, Phase-field models in materials science, Modell. Simul. Mater. Sci. Eng. 17 (7) (2009) 073001.
[31] M. Fleck, L. Mushongera, D. Pilipenko, K. Ankit, H. Emmerich, On phase-field modeling with a highly anisotropic interfacial energy, Eur. Phys. J. Plus 126 (2011) 1–11.
[32] Y. Chen, J. Lowengrub, J. Shen, C. Wang, S. Wise, Efficient energy stable schemes for isotropic and strongly anisotropic cahn–Hilliard systems with the willmore regularization, J. Comput. Phys. 365 (2018) 56–73.
[33] O. Tschukin, A. Silberzahn, M. Selzer, P.G.K. Amos, D. Schneider, B. Nestler, Concepts of modeling surface energy anisotropy in phase-field approaches, Geotherm. Energy 5 (2017) 1–21.
[34] N. Nguyen-Thanh, W. Li, J. Huang, K. Zhou, Multi phase-field modeling of anisotropic crack propagation in 3D fiber-reinforced composites based on an adaptive isogeometric meshfree collocation method, Comput. Methods Appl. Mech. Eng. 393 (2022) 114794.
[35] M.R. Khosravani, S. Rezaei, H. Ruan, T. Reinicke, Fracture behavior of anisotropic 3D-printed parts: experiments and numerical simulations, J. Mater. Res. Technol. 19 (2022) 1260–1270.
[36] J.-M. Scherer, S. Brach, J. Bleyer, An assessment of anisotropic phase-field models of brittle fracture, Comput. Methods Appl. Mech. Eng. 395 (2022) 115036.
[37] X. Zou, Z. Xu, J. Gao, S. Wu, R. Li, W. Li, X. He, An explicit multi-phase field damage model for long fiber-reinforced composites, Compos. Struct. 309 (2023) 116737.
[38] I. Jain, A. Muixí, C. Annavarapu, S.S. Mulay, A. Rodríguez-Ferran, Adaptive phase-field modeling of fracture in orthotropic composites, Eng. Fract. Mech. 292 (2023) 109673.
[39] A. Mitrou, A. Arteiro, J. Reinoso, P.P. Camanho, Modeling fracture of multidirectional thin-ply laminates using an anisotropic phase field formulation at the macro-scale, Int. J. Solids Struct. 273 (2023) 112221.
[40] N. Nguyen-Thanh, H. Nguyen-Xuan, W. Li, Phase-field modeling of anisotropic brittle fracture in rock-like materials and polycrystalline materials, Comput. Struct. 296 (2024) 107325.
[41] J. He, T. Yu, W. Fang, S. Natarajan, Dynamic crack growth in orthotropic brittle materials using an adaptive phase-field modeling with variable-node elements, Compos. Struct. 337 (2024) 118068.
[42] A. Bijaya, S. Sagar, S.R. Chowdhury, A consistent multi-phase-field formulation for anisotropic brittle fracture, Eng. Fract. Mech. 295 (2024) 109825.
[43] A. Kumar, T. Sain, A 3D multi-phase-field model for orientation-dependent complex crack interaction in fiber-reinforced composite laminates, Eng. Fract. Mech. 303 (2024) 110097.
[44] A. Kumar, T. Sain, Modeling the interaction between intra and interlaminar cracking in FRP composites using phase-field regularized interface fracture, Theor. Appl. Fract. Mech. 129 (2024) 104177.
[45] W. Yuan, Y. Zhao, B. Zhang, A stress-Driven double-Phase–Field framework for tensile fracturing processes in transversely isotropic rocks, Int. J. Numer. Anal. Methods Geomech. 48 (17) (2024) 4188–4205.
[46] Y. Yu, C. Hou, X. Zheng, M. Zhao, Phase field modeling for composite material failure, Fatigue Fract. Eng. Mater. Struct. 47 (11) (2024) 4176–4195.
[47] Z. Liu, P. Lenarda, J. Reinoso, M. Paggi, Phase field modeling of anisotropic silicon crystalline cracking in 3D thin-walled photovoltaic laminates, Int. J. Fract. 249 (1) (2025) 1–19.
[48] N. Prajapati, C. Herrmann, M. Späth, D. Schneider, M. Selzer, B. Nestler, Brittle anisotropic fracture propagation in quartz sandstone: insights from phase-field simulations, Comput. Geosci. 24 (2020) 1361–1376.
[49] C. Herrmann, D. Schneider, E. Schoof, F. Schwab, B. Nestler, Phase-field model for the simulation of brittle-anisotropic and ductile crack propagation in composite materials, Materials 14 (17) (2021) 4956.
[50] M. Späth, C. Herrmann, N. Prajapati, D. Schneider, F. Schwab, M. Selzer, B. Nestler, Multiphase-field modelling of crack propagation in geological materials and porous media with drucker-Prager plasticity, Comput. Geosci. 25 (2021) 325–343.
[51] S. Rezaei, A. Harandi, T. Brepols, S. Reese, An anisotropic cohesive fracture model: advantages and limitations of length-scale insensitive phase-field damage models, Eng Fract Mech 261 (2022) 108177.
[52] L. Ambrosio, V.M. Tortorelli, Approximation of functional depending on jumps by elliptic functional via t-convergence, Commun. Pure Appl. Math. 43 (8) (1990) 999–1036.
[53] W. Voigt, Über die beziehung zwischen den beiden elastizitätskonstanten isotroper körper, Wied. Ann. 38 (12) (1889) 573–587.
[54] D. Schneider, E. Schoof, O. Tschukin, A. Reiter, C. Herrmann, F. Schwab, M. Selzer, B. Nestler, Small strain multiphase-field model accounting for configurational forces and mechanical jump conditions, Comput. Mech. 61 (3) (2018) 277–295.
[55] C. Miehe, M. Hofacker, F. Welschinger, A phase field model for rate-independent crack propagation: robust algorithmic implementation based on operator splits, Comput. Methods Appl. Mech. Eng. 199 (45–48) (2010) 2765–2778.
[56] B. Bourdin, G.A. Francfort, J.-J. Marigo, Numerical experiments in revisited brittle fracture, J. Mech. Phys. Solids 48 (4) (2000) 797–826.
[57] L. Schöller, D. Schneider, C. Herrmann, A. Prahs, B. Nestler, Phase-field modeling of crack propagation in heterogeneous materials with multiple crack order parameters, Comput. Methods Appl. Mech. Eng. 395 (2022) 114965.
[58] M.F. Wheeler, T. Wick, W. Wollner, An augmented-Lagrangian method for the phase-field approach for pressurized fractures, Comput. Methods Appl. Mech. Eng. 271 (2014) 69–85.
[59] T. Heister, M.F. Wheeler, T. Wick, A primal-dual active set method and predictor-corrector mesh adaptivity for computing fracture propagation using a phase-field approach, Comput. Methods Appl. Mech. Eng. 290 (2015) 466–495.
[60] K. Mang, T. Wick, W. Wollner, A phase-field model for fractures in nearly incompressible solids, Comput. Mech. 65 (1) (2020) 61–78.
[61] J. Wambacq, J. Ulloa, G. Lombaert, S. François, Interior-point methods for the phase-field approach to brittle and ductile fracture, Comput. Methods Appl. Mech. Eng. 375 (2021) 113612.
[62] J. Hötzer, A. Reiter, H. Hierl, P. Steinmetz, M. Selzer, B. Nestler, The parallel multi-physics phase-field framework pace3d, J. Comput. Sci. 26 (2018) 1–12.
[63] B. Li, C. Maurini, Crack kinking in a variational phase-field model of brittle fracture with strongly anisotropic surface energy, J. Mech. Phys. Solids 125 (2019) 502–522.
[64] V. Hakim, A. Karma, Crack path prediction in anisotropic brittle materials, Phys. Rev. Lett. 95 (23) (2005) 235501.
[65] J.E. Taylor, J.W. Cahn, Diffuse interfaces with sharp corners and facets: phase field models with strongly anisotropic surfaces, Physica D 112 (3–4) (1998) 381–411.
[66] M.E. Gurtin, P. Podio-Guidugli, Configurational forces and a constitutive theory for crack propagation that allows for kinking and curving, J. Mech. Phys. Solids 46 (8) (1998) 1343–1378.

[67] M. Amestoy, J.-B. Leblond, Crack paths in plane situations–II. detailed form of the expansion of the stress intensity factors, Int. J. Solids Struct. 29 (4) (1992) 465–501.
[68] N. Zhu, E. Oterkus, Calculation of stress intensity factor using displacement extrapolation method in peridynamic framework, J. Mech. 36 (2) (2020) 235–243.
[69] D. Schneider, O. Tschukin, A. Choudhury, M. Selzer, T. Böhlke, B. Nestler, Phase-field elasticity model based on mechanical jump conditions, Comput. Mech. 55 (5) (2015) 887–901.
[70] C. Herrmann, E. Schoof, D. Schneider, F. Schwab, A. Reiter, M. Selzer, B. Nestler, Multiphase-field model of small strain elasto-plasticity according to the mechanical jump conditions, Comput. Mech. 62 (6) (2018) 1399–1412.
[71] A.T. Zehnder, Fracture Mechanics, 62, Springer Science & Business Media, 2012.